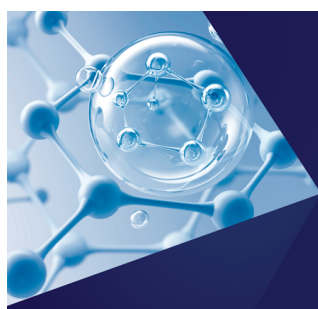# Core level photoelectron spectroscopy of heterogeneous reactions at liquid–vapor interfaces: Current status, challenges, and prospects 🅕

Rémi Dupuy ⬡ ; Clemens Richter ⬡ ; Bernd Winter ⬡ ; Gerard Meijer ⬡ ; Robert Schlögl; Hendrik Bluhm ✉ ⬡

Check for updates

View Online

Export Citation

07 May 2025 10:15:31

Core level photoelectron spectroscopy of heterogeneous reactions at liquid–vapor interfaces: Current status, challenges, and prospects (F)

Rémi Dupuy, (iD) Clemens Richter, (iD) Bernd Winter, (iD) Gerard Meijer, (iD) Robert Schlögl,
and Hendrik Bluhm[a] (iD)

AFFILIATIONS

Fritz Haber Institute of the Max Planck Society, Faradayweg 4-6, D-14195 Berlin, Germany

[a]Author to whom correspondence should be addressed: bluhm@fhi-berlin.mpg.de

ABSTRACT

Liquid–vapor interfaces, particularly those between aqueous solutions and air, drive numerous important chemical and physical processes in the atmosphere and in the environment. X-ray photoelectron spectroscopy is an excellent method for the investigation of these interfaces due to its surface sensitivity, elemental and chemical specificity, and the possibility to obtain information on the depth distribution of solute and solvent species in the interfacial region. In this Perspective, we review the progress that was made in this field over the past decades and discuss the challenges that need to be overcome for investigations of heterogeneous reactions at liquid–vapor interfaces under close-to-realistic environmental conditions. We close with an outlook on where some of the most exciting and promising developments might lie in this field.

I. INTRODUCTION

The liquid–vapor interface is of profound scientific, environmental, technological, and public health interest. The most important liquid–vapor interface is arguably that between aqueous solutions and the surrounding air, which drives significant processes in the environment. One example is the uptake of CO_2 at the ocean–air interface, which has an estimated area of 3.6×10^8 km^2. About one third of the anthropogenically generated CO_2 is sequestered at this interface.[1] Of similar importance are the uptake and release of trace gas molecules by aqueous aerosols, for instance, cloud and fog droplets, and the ensuing reactions. The estimated total volume of condensed water in the atmosphere[2] is about 1.3×10^4 km^3; assuming an average droplet diameter[3] of 10 μm, the total surface area of aqueous aerosols exceeds that of the oceans' by several orders of magnitude, emphasizing the importance of aerosol heterogeneous chemistry for atmospheric and environmental processes. In addition, aerosols are involved in the transmission

of pathogens and have recently attracted increased attention in connection with the spread of SARS-COV-2.[4]

For a fundamental understanding of heterogeneous reactions at liquid–vapor interfaces, experimental and theoretical techniques are needed that are able to cope with the dynamic nature of the fluxional interface and provide information on its chemical composition and physical nature on the molecular scale. Investigations of liquid–vapor interactions often require that the experiments are performed at elevated pressures, far away from ultra-high vacuum conditions prevalent in traditional surface science studies. This is particularly true for studies of aqueous interfaces at environmentally relevant temperatures. Thus, the general challenges for experiments at liquid–vapor interfaces are similar to those in experiments on solid–vapor interfaces, especially model studies of heterogeneous catalytic reactions. However, while investigations of solid–vapor interfaces have been pursued for a wide range of sample materials, structures, and reactions for many decades,[5–8] there is a much smaller body of work for liquid–vapor interfaces. This is partly

due to the difficulties posed by the preparation of well-controlled contamination-free model liquid–vapor interfaces and their investigation with surface-sensitive probes.

The scope of this Perspective is the application of core level photoelectron spectroscopy, which provides surface-sensitive elemental and chemical information, for the investigation of liquid–vapor interfaces. We will review the development of the experimental capabilities over the past decades and give examples for new developments in this field, including technical hurdles that need to be overcome for a more general applicability of core level photoelectron spectroscopy for studies of heterogeneous chemical reactions at liquid–vapor interfaces under realistic conditions.

Some of the chief scientific questions regarding liquid–vapor interfaces concern (i) the chemical composition at the interface vs the composition of the bulk liquid phase, (ii) the fundamental steps during the uptake and release of trace gases, (iii) the formation and the fate of reaction products at the interface and their potential transport into the bulk phase, (iv) the role of surfactants, which can suppress or increase the interaction between gas phase and solution species or participate in the reaction directly, and (v) the dependence of these processes on conditions such as temperature, reactant velocity, reactant orientation, and the nature of the reactive chemical species (see Fig. 1).

A wealth of information on the heterogeneous chemistry at liquid–vapor interfaces has been obtained over the past decades using flow reactor studies, where aerosol droplets are exposed to reactive gases and the gas phase composition at the reactor outlet is compared to that at the inlet.[9,10] When the cumulative area of all aerosols in the reactor is known, quantitative information on the uptake coefficients as well as reaction rates and products can be obtained. While these kinds of studies by their nature give an indirect view of interfacial reactions, they provided the first indications that some halide ions (such as I^- and Br^-) are most likely

residing close to the liquid–vapor interface,[11] contrary to earlier predictions from surface tension measurements[12] and electrostatic considerations[13] that predicted that the interfacial region is devoid of ions.

A wide variety of techniques has been used for surface-specific investigations of liquid–vapor interfaces. Historically, one of the main characterization techniques has been the surface tension measurement using the Wilhelmy method.[14,15] This is essentially a macroscopic measurement that often requires modeling the effect of solutes on the surface tension to provide information on quantities such as the surface excess of molecules. These measurements can be combined with imaging methods such as Brewster angle microscopy,[16] which provides information on the homogeneity and 2D morphology of surfactant films on the sub-mm lengths scale.

In the past 40 years, many more methods, a lot of which were adapted from solid-state surface science, have been applied to characterize liquid–vapor interfaces at the molecular level (see Ref. 17 and references therein). Among these are linear and nonlinear optical vibrational spectroscopies:[18] infrared reflection–absorption spectroscopy (IRRAS,[19–22] often called RAIRS in surface science[23]), grazing angle Raman (GAR),[18] vibrational sum-frequency generation (VSFG),[24–26] and second-harmonic generation (SHG).[26] These techniques mainly provide information on the nature and orientation of species at the interface and on the hydrogen-bonding network.

Another class of characterization methods are hard x-ray based diffraction techniques.[27,28] X-ray reflectivity[27,28] (XR) probes the electron density profile along the surface normal, which can be interpreted in terms of molecular arrangements, depth distributions, and surface roughness, while grazing incidence x-ray diffraction (GIXD) and small angle scattering at grazing incidence[28] (GISAXS) probe also the in-plane properties of the surface and provide information on surface ordering and molecular orientation. Resonant variants of these techniques can achieve elemental specificity. An additional x-ray based technique probing elemental composition is x-ray fluorescence near total reflection[27] (XFNTR), which is the measurement slightly above and below the total reflection angle of the (element-specific) x-ray fluorescence, giving bulk and surface-sensitive information, respectively. Finally, surface X-ray Photon Correlation Spectroscopy[28] (XPCS) is used to dynamically probe surface capillary waves through the analysis of an x-ray speckle pattern.

In the (mostly) soft x-ray range, x-ray absorption spectroscopy (XAS) techniques have been used to probe unoccupied electronic states of liquids and solutions in electron and fluorescent yield modes.[29–32] A particular focus of these studies has been on the hydrogen-bonding network in water[33,34] and the influence of the presence of solutes on it in aqueous solutions.[32,35,36] A related method is x-ray Raman spectroscopy,[37] which, like the more recently used Resonant Inelastic X-ray Scattering (RIXS),[38–40] was also employed to obtain specific information on the chemical nature and environment of the probed atom, but since both methods rely on the detection of photons, they are less surface-sensitive.

Ion scattering techniques have also been employed to study liquid–vapor interfaces.[41,42] High energy (MeV or above) techniques such as Rutherford Backscattering (RBS) or Elastic Recoil Detection Analysis (ERDA) are less surface-sensitive due to their
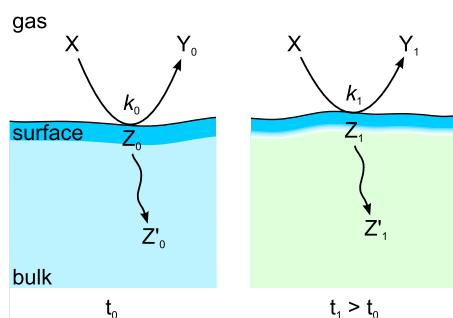
FIG. 1. Schematic representation of some of the fundamental processes that may occur at liquid–vapor interfaces. In this example, a vapor phase species X reacts with a rate constant k_0 at time t_0 with solution species to form a product Z_0 at the interface and possibly also a new vapor species Y_0. If Z_0 is soluble, it will diffuse over time into the bulk. The different blue shading of the bulk and the surface region indicates that even in the absence of surface reactions, the chemical composition of the interface region may be different from that of the bulk. The continued reaction of the gas phase with the solution species can, over time, change the chemical composition of the bulk and the surface region, as shown here in the vignette for t_1. This, in turn, may then change the nature of the surface and bulk reactions.

07 May 2025 10:15:31

high probing depth (typically 1 μm). However, their low-energy (1 keV–10 keV) counterparts are used to investigate the interface. The detection of backscattered ions—low-energy ion scattering (LEIS), impact collision ion scattering spectroscopy (ICISS), or direct recoil spectroscopy (DRS)—probes the elemental composition of the outermost layer. Detection of the 180° backscattered neutrals, as in neutral impact collision ion scattering spectroscopy (NICISS), has further utility since it can be used to obtain depth profiles of the chemical composition across the interface.

A related method is molecular beam scattering,[43] which provides information on the presence of solutes right at the interface, but perhaps even more important is a powerful method for the study of heterogeneous reactions. Particles are typically detected using a quadrupole mass spectrometer, providing information on the nature and velocity of the scattered molecules, but additionally, laser-based spectroscopic techniques can be applied to measure their rotational, vibrational, and electronic state populations.[44] It is also an excellent method to determine the interaction times between gas molecules and surface species and has been used to show that surfactants can both enhance and decrease the uptake of gas molecules at the liquid–vapor interface.[45]

Among electron spectroscopy techniques, metastable induced electron spectroscopy[42] (MIES) is used to determine the valence electronic structure [binding energy (BE) <20 eV] and molecular orientation with a high surface sensitivity, i.e., the electronic density about 2 Å above the outermost layer is probed. However, the stringent vacuum requirement for MIES is an obstacle to its wide-spread application. The same can be said for electron energy loss spectroscopy (EELS), which—to the best of our knowledge—has only been applied once to the measurement of liquids.[46]

In this Perspective, we focus on the investigation of liquid–vapor interfaces by core level x-ray photoelectron spectroscopy (XPS),[47] which is complementary to the above-listed techniques since it provides direct information on the elemental and chemical composition of a surface (e.g., functional groups and oxidation state). Its high surface-sensitivity is due to the short mean free path of electrons at typical electron kinetic energies (KE) in XPS experiments, i.e., a few tens to hundreds of eV. At these KEs, the information depth is on the order of a few nanometers, although the precise values for aqueous solutions are still under debate, as will be discussed below. Through variation of the detection angle with respect to the surface, or the photoelectron kinetic energy for a given core level, the probing depth in an XPS experiment can be varied, and thus, surface-bound species can be distinguished from those in the bulk. XPS is therefore ideally suited to measure differences in the surface and bulk chemical concentrations at liquid–gas interfaces and to monitor heterogeneous chemical reactions. This Perspective focuses on core level XPS used as a chemical composition analysis technique and will not cover related photoemission techniques such as resonant photoemission spectroscopy and valence photoemission spectroscopy; refer to the reviews by Thürmer *et al.*[48] and Seidel *et al.*,[49] respectively.

Investigations at liquid–vapor interfaces using XPS pose specific challenges since (contrary to most solid materials) liquids—and particularly aqueous solutions—have a significant vapor pressure under environmentally relevant conditions. One exception is ionic liquids,[50,51] which have almost negligible vapor pressures at room temperature and can even be studied under ultra-high vacuum

conditions, which will not be covered here. The vapor pressure of water is about 6 mbar at the triple point and about 30 mbar at 25 °C. XPS measurements at these pressures require experimental strategies that minimize the scattering of electrons by gas molecules, as this otherwise leads to the attenuation of the detected photoelectron signal. There are two main approaches to overcome this obstacle: for one, the background pressure can be reduced by many orders of magnitude in experiments using fast flowing jets[52] or droplet trains,[53] which are frozen out rapidly after the liquid jet was probed by XPS. This is a versatile approach for investigations of the interface chemical composition of solutions or for fast reactions, as discussed below.

The other approach is used for studies of heterogeneous reactions at liquid–vapor interfaces under steady-state conditions, where the measurements are ideally performed in the presence of the equilibrium vapor pressure of the solution and the relevant trace gas pressures, i.e., at elevated pressures. XPS can be adapted to operation under non-vacuum conditions through the utilization of differential pumping stages that reduce the path length of the electrons through the gas phase and thus, in turn, reduce scattering of the electrons and signal attenuation. This adaptation of XPS, commonly named ambient pressure XPS (APXPS) or near-ambient pressure XPS (NAP-XPS), was developed first by the Siegbahn group in Uppsala in the early 1970s.[54] APXPS has steadily evolved over the past decades to where it can now be operated even above 1 atm[55–59] under certain conditions, which, however, do not easily lend themselves for measurements of liquid–vapor interfaces, as discussed below.

The pressure range of interest for experiments of heterogeneous reactions at aqueous solution–vapor interfaces is given by the sum of the equilibrium solution vapor pressure and that of the trace gases of interest, of which CO_2 has the highest partial pressure in the environment currently at 0.4 mbar. The required pressure in APXPS investigations of heterogeneous reactions of aqueous solutions in the environment at room temperature is thus around 30 mbar in total, if one assumes that the other majority gases in the atmosphere, O_2, N_2, and Ar, play a negligible role in these reactions. Most standard APXPS instruments are now able to operate at these water vapor pressures, aided also by the fact that water molecules are relatively weak electron scatterers compared to most other common gases. APXPS is thus an excellent method to study the heterogeneous chemistry of aqueous solutions and the distribution of solvent, solute, and surfactant species across the liquid–vapor interface.

Figure 2 displays a timeline of XPS experiments on liquid–vapor interfaces since the early works by the Siegbahn group at Uppsala. The publications in the plot are subdivided by some of the main preparation techniques for liquid–vapor interfaces (colors, discussed below) as well as whether the experiments were done by the suppression of the background vapor pressure (full color) or by the ambient pressure XPS (shaded areas). Figure 2 and Table I (to be introduced later) show that the early experiments were mostly done using APXPS on the wetted surfaces of trundles and disks in the presence of the equilibrium vapor pressure, while the development of liquid microjets in combination with tightly focused synchrotron-based x rays laid the foundation for the more recent surge in measurements on liquid–vapor interfaces, the vast majority of which were performed under high-vacuum conditions. Early

07 May 2025 10:15:31
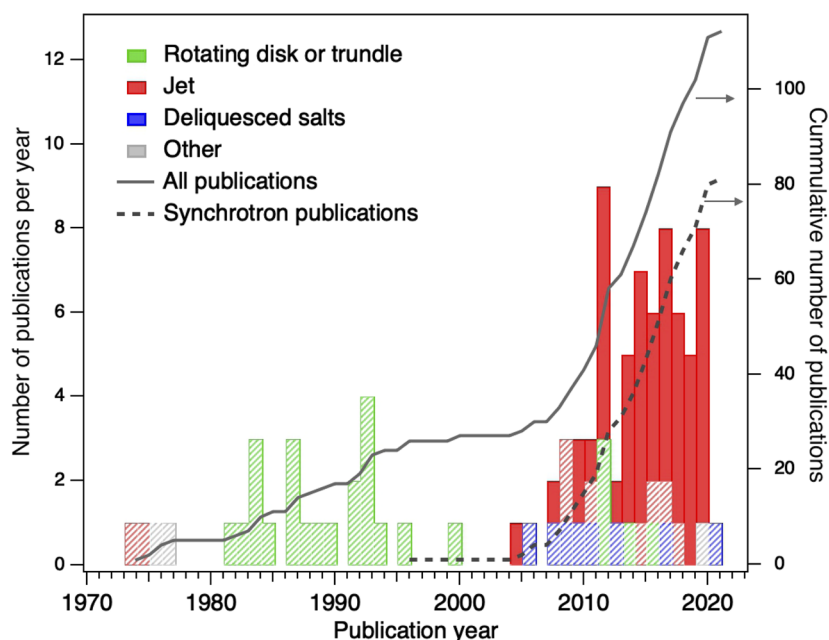
FIG. 2. Peer-reviewed original publications of XPS studies on liquid–vapor interfaces sorted by the preparation method for the liquid interface. Shaded areas indicate the fraction of studies that were performed in quasi-equilibrium, i.e., at the vapor pressure of the solution at the given temperature. Fully colored areas indicate studies where the background vapor pressure is strongly reduced through freezing-out of the solution after the XPS measurement. The solid line indicates the cumulative total number of publications over the past decades, starting from the first measurements at Uppsala University. The broken line shows the cumulative number of publications that resulted from experiments using synchrotron sources; these experiments have clearly gained importance over the past decade. This statistic only includes publications focusing on conventional XPS studies on core levels. Studies with particular focus on the valence electronic structure have been excluded as these deserve a separate review.

TABLE I. Published XPS and APXPS investigations of liquid–vapor interfaces.[a]

Solvent	Solute(s)	Pressure (mbar)[b]	Equil.[c]	Year	Reference	Facility
Liquid jet						
Formamide	Pure, KI	$<10^{-2}$ (NS)	No	1973	54	Lab (Uppsala)
Formamide		$<10^{-2}$ (NS)	No	1974	103	Lab (Uppsala)
Formamide, ethylene glycol, benzyl alcohol	Formamide, ethylene glycol, benzyl alcohol	$<10^{-2}$ (NS)	No	1975	104	Lab (Uppsala)
Water	TBAI	10^{-5}	No	2004	105	BESSY
Water	TBAI, NaBr	10^{-5}	No	2005	106	BESSY
Water	Lysine	10^{-5}	No	2007	107	BESSY
Water	TBAI	10^{-5}	No	2007	108	MAX-lab
Water		10^{-5}	No	2007	109	BESSY
Water	KF	5	Yes	2008	110	ALS
Water	Imidazole	10^{-5}	No	2008	111	BESSY
Water	NaCl, NaClO, NaClO$_2$, NaClO$_3$, NaClO$_4$	10^{-5}	No	2009	112	BESSY
Water	NaOH	10^{-4}	No	2009	113	BESSY
Water	NaNO$_3$, NaNO$_2$	NS	No	2009	114	BESSY
Water	LiBr, LiI, NaBr, NaCl	NS	No	2010	115	MAX-lab
Water	NaCl, MgCl$_2$, AlCl$_3$	NS	No	2010	116	MAX-lab
Water	NaI	10^{-4}	No	2010	117	BESSY
Water	SiO$_2$ nanoparticles	10^{-4}	No	2011	118	BESSY

07 May 2025 10:15:31

TABLE I. *(Continued.)*

Solvent	Solute(s)	Pressure (mbar)[b]	Equil.[c]	Year	Reference	Facility
Water	H_2O_2	10^{-4}	No	2011	119	BESSY
Water	Glycine	NS	No	2011	120	MAX-lab
Water	Formic, acetic, butyric acid	NS	No	2011	121	MAX-lab
Water	SiO_2 nanoparticles (func.)	NS	No	2011	122	MAX-lab
Water	HNO_3	1.5×10^{-4}	No	2011	123	BESSY
Water		10^{-4}	No	2011	124	Spring-8
Water	$NaNO_3$, HNO_3	1.5×10^{-4}	No	2011	125	BESSY
Water	MEA, CO_2	1.5×10^{-4}	No	2011	126	BESSY
Water	HCOOH	10^{-5}	No	2012	127	BESSY
Water	NaDecanoate, NaCl, Na_2SO_4, $(NH_4)_2SO_4$, NH_4Cl	NS	No	2012	128	MAX-lab
Water, acetonitrile, ethanol	LiI_3, LiI	10^{-5}	No	2013	129	MAX-lab
Water	SiO_2 nanoparticles	10^{-4}	No	2013	130	BESSY
Water	H_2SO_4	10^{-4}	No	2013	131	BESSY
Water	NaCl, lysine	10^{-4}	No	2013	132	Spring-8
Water		10^{-4}	No	2013	133	BESSY
Water, acetonitrile		10^{-5}, 1.3	Both	2014	92	BESSY, ALS
Water	HCOOH, NaCl	10^{-4}	No	2014	134	SLS
Water	KF, KCl, KBr	NS	No	2014	135	MAX-lab
Water	Succinic acid	NS	No	2014	136	MAX-lab
Water	GdmCl, NaCl, NH_4Cl	NS	No	2014	137	MAX-lab
Water	NaCl, NaBr, NaI	10^{-4}	No	2014	138	Spring-8, lab
Water	NaCl	NS	No	2014	139	Spring-8
Water	Trichloroethanol	10^{-5}	No	2014	140	MAX-lab
Water, acetonitrile, ethanol	LiI_3, LiI	NS	No	2015	141	MAX-lab
Water	K_2CO_3	10^{-4}, 6	Both	2015	93	SLS
Water	NaOctanoate, NaPropionate, NH_4Cl	NS	No	2015	142	MAX-lab
Water	NaBr, citric acid	10^{-4}	No	2015	143	SLS
Water	$TiCl_3$	10^{-4}	No	2015	144	BESSY
Water	1-pentanol, 3-pentanol	NS	No	2015	145	MAX-lab
Water	Alcohols (C_1–C_4), carboxylic acids (C_1–C_4)	10^{-4}	No	2016	146	SLS
Water	1-butanol, tert-butanol, 1-pentanol, 3-pentanol, 1-hexanol, 3-hexanol	NS	No	2016	147	MAX-lab
Water	Succinic acid, NaCl, NH_4Cl	NS	No	2016	148	MAX-lab
Water	TiO_2 nanoparticles, HNO_3	1.3	Yes	2016	149	ALS
Water	Al_xO_x/SiO_2 core–shell NPs	10^{-4}	No	2016	150	SLS
Water	HCOOH, Al_xO_x/SiO_2 core–shell NPs	10^{-4}	No	2016	151	SLS
Water	NaCl	10^{-4}	No	2016	152	SLS
Water	Br^-, O_3	10^{-3}–0.3	No	2017	153	SLS
Water	$[Co(CN)_6]K_3$	10^{-4}	No	2017	154	BESSY
Water	Na_2CO_3, $NaHCO_3$, H_2CO_3	10^{-2}	No	2017	155	ALS
Water	LiI, KI	1	Yes	2017	156	ALS
Water	$FeCl_3$, NaOH	10^{-4}	No	2017	157	BESSY
Water	LiCl	10^{-4}	No	2017	158	BESSY
Water	Fe_2O_3 nanoparticles	7.5×10^{-4}	No	2018	159	BESSY
Water	GdmCl, TPACl, Na_2SO_4, NaCl	NS	No	2018	160	MAX-lab
Water	Hexylammonium chloride, NaHexanonate	NS	No	2018	161	MAX-lab
Water	Butyric, pentanoic acid, butyl, hexyl amine, NaOH, HCl	NS	No	2018	162	MAX-lab
Water	NaCl, NaBr, NaI	10^{-4}	No	2018	163	SLS

07 May 2025 10:15:31

TABLE I. *(Continued.)*

Solvent	Solute(s)	Pressure (mbar)[b]	Equil.[c]	Year	Reference	Facility
Water	NaBr, NaI, 1-butanol, butyric acid	10^{-3}	No	2019	164	SLS
Water	TiO_2 NPs, HCl, HNO_3, NH_4OH	3×10^{-3}	No	2019	165	BESSY
Water	DMS, DMSO, $DMSO_2$, $DMSO_3$	1.5×10^{-4}	No	2019	166	BESSY
Water	Carboxylic acids (C_1–C_8), NH_3	NS	No	2019	167	MAX-lab
Water	Cysteine	10^{-4}	No	2019	168	MAX-lab, LNLS
Ammonia	Pure	4×10^{-3}	No	2019	60	BESSY
Water	NaI, TBAI, NH_3Cl	NS	No	2019	169	Spring-8, lab
Water	H_2SO_4, $FeSO_4$	5×10^{-4}	No	2019	170	Lab (irvine)
Ammonia	KI, NH_4I	10^{-3}	No	2020	61	BESSY
Ammonia	Li, Na, K	10^{-3}	No	2020	62	BESSY
Droplet train						
Water	Methanol	5	Yes	2008	53	ALS
Moving wire						
Ethylene glycol		10^{-1}	Yes	1975	171	Lab (Uppsala)
Ethylene glycol	N-methyl-glucamine salts	NS	Yes	1976	172	Lab (Uppsala)
Rotating trundle						
Ethanol, methanol	NaI, I_2	NS	Yes	1981	173	Lab (Uppsala)
Formamide	Pure		Yes	1982	174	Lab (Uppsala)
Glycol	Ag^+, Cu^+, Zn^{2+}	NS	Yes	1983	175	Lab (Uppsala)
Glycol	Na^+, K^+, Rb^+, Cs^+	NS	Yes	1983	176	Lab (Uppsala)
Ethanol	NaI, I_2	NS	Yes	1983	177	Lab (Uppsala)
Glycol, ethanol	Mg^{2+}, Ca^{2+}, $Sr.^{2+}$, Ba^{2+}, Ag^+, Zn^{2+}, Cd^{2+}, Hg^{2+}, Mn^{2+}	NS	Yes	1984	178	Lab (Uppsala)
Glycol	F^-, Cl^-, Br^-, I^-, I_2, I_3^-, NO_3^-	NS	Yes	1984	179	Lab (Uppsala)
Water	LiCl, glycol, dimethylformamide	0.1–1	Yes	1986	180	Lab (Uppsala)
Tetramethyl guanidine	NaI, water	NS	Yes	1986	181	Lab (Uppsala)
Formamide	TBAI	NS	Yes	1986	182	Lab (Uppsala)
Formamide	Octanol, bromooctanol	4×10^{-2}	Yes	1987	183	Lab (Uppsala)
Formamide	Tetra-N-alkylammonium salts	NS	Yes	1988	184	Lab (Uppsala)
Heptane	Butyllithium	NS	Yes	1989	185	Lab (Uppsala)
Glycol	NaOH, Be^{2+}	NS	Yes	1992	186	Lab (Uppsala)
Rotating disk						
Formamide	TBA salts, ($IPrNBu_3$)I	NS	Yes	1991	187	Lab (Uppsala)
Formamide	Potassium octanoate, potassium 11-bromoundecanoate	NS	Yes	1991	188	Lab (Uppsala)
Formamide, ethylene glycol	Potassium octanoate	NS	Yes	1992	189	Lab (Uppsala)
Formamide	TBABr, Tributyl(bromomethyl)NBr, NH_4Cl	NS	Yes	1992	190	Lab (Uppsala)
Formamide	TBABr, TBPBr	NS	Yes	1992	191	Lab (Uppsala)
Formamide, ethylene glycol	Potassium octanoate	NS	Yes	1993	192	Lab (Uppsala)
Formamide	CsI, $TBANO_3$, potassium octanoate	NS	Yes	1995	193	Lab (Uppsala)
Formamide	CsI, $TBANO_3$	NS	Yes	1999	194	Lab (Uppsala)
Formamide	TBACl	NS	Yes	2010	195	Lab (leipzig)
Formamide	TBPBr	NS	Yes	2011	196	Lab (leipzig)
Formamide	TBAI	NS	Yes	2011	197	Lab (leipzig)
Formamide	TBAI	NS	Yes	2011	198	Lab (leipzig)
HPN	POPC, TBABr	NS	Yes	2013	199	Lab (leipzig)

07 May 2025 10:15:31

TABLE I. *(Continued.)*

Solvent	Solute(s)	Pressure (mbar)[b]	Equil.[c]	Year	Reference	Facility
Liquid lamella						
Formamide	TBAI	10^{-4}	No	1995	94	BESSY
Static droplet						
Propylene carbonate	LiClO$_4$	2×10^{-1}	Yes	2015	200	MAX-lab
Propylene carbonate	LiTFSI	2×10^{-1}	Yes	2019	201	MAX-lab
Deliquesced salt						
Water	KBr, KI	2	Yes	2005	202	ALS
Water	KI, butanol	2	Yes	2007	203	ALS
Water	NaCl, Br	2	Yes	2008	204	ALS
Water	NaCl, NaClO$_4$	5	Yes	2009	205	ALS
Water	NaCl	0.1–1	Yes	2010	206	ALS
Water	NaCl, RbCl, RbBr	5	Yes	2012	207	ALS
Water	NaCl, NaBr, NaI	8	Yes	2015	208	SOLEIL
Water	NaCl, NaI	8	Yes	2016	209	SOLEIL
Water	NaAcetate	0.7	Yes	2020	210	SLS

[a]Included in this table are all APXPS papers on liquid–vapor interfaces that we know of, as of May 2020. To keep the scope of this table to a reasonable size, we exclude studies performed at background pressures lower than 10^{-5} mbar (most notably, XPS studies of ionic liquids or pre-melted liquids) and studies focusing mostly on resonant/Auger emission spectroscopy or valence band PES (binding energies <50 eV).

[b]Background vapor pressure of the experiment. NS = non-stated.

[c]Indicates whether the liquid surface is in equilibrium with the vapor pressure in the experiment.

experiments used polar organic solvents—mostly formamide—with low vapor pressures, while recent ones focused almost entirely on aqueous solutions. Very recently, the use of XPS on liquids that are more challenging to handle, such as liquid ammonia, has been demonstrated as well.[60–62]

The overwhelming number of published XPS measurements on liquid–vapor interfaces summarized in Fig. 2 have focused on the chemical composition and depth distribution at liquid–vapor interfaces in the absence of heterogeneous reactions with gaseous species. Several of these works have been reviewed previously. XPS experiments on liquid–vapor interfaces, and related topics, such as valence photoemission or Auger electron spectroscopy, were reviewed in 2006 by Winter and Faubel,[52] in 2009 by Brown *et al.*,[63] in 2009 by Winter,[64] in 2011 by Seidel *et al.*,[65] and more recently in 2018 by Ammann *et al.*[66] A 2016 review by Seidel *et al.*[49] covers specifically valence band photoemission spectroscopy. The early work of the Uppsala group has been reviewed by Siegbahn[67] as well as in several other reviews cited above. The specific topic of nanoparticles in solution has been discussed by Brown *et al.*[68] The work of Morgner and co-workers was reviewed in a recent book chapter by Andersson and Morgner.[42]

The aim of this Perspective is to describe the progress that has been made so far in photoelectron spectroscopy experiments on liquid–vapor interfaces and specifically discuss the challenges that lie ahead for a systematic investigation of heterogeneous reactions at liquid–vapor interfaces, including the interplay between the interfacial and bulk concentration of educts and products of the reaction. We also discuss some of the prospects for future investigations of liquid–vapor interfaces, where, especially, pump–probe-type experiments at the shorter time scale and studies on well-controlled surfactant layers as a function of their packing and chemistry will open up opportunities for a fundamental molecular-scale understanding of heterogeneous processes at liquid–vapor interfaces across a wide range of time scales and chemical compositions.

II. EXPERIMENTAL CONSIDERATIONS

In this section, we discuss some of the experimental foundations of XPS experiments on liquid–vapor interfaces, including a description of the different methods that are applicable for the preparation of these interfaces inside vacuum chambers. We also describe specific challenges in the data analysis of XPS experiments on liquid–vapor interfaces, such as the quantitative determination of depth profiles across the interface and the calibration of the photoelectron binding energy. We start with a brief review of XPS and APXPS.

A. XPS and ambient pressure XPS

XPS is one of the most powerful methods for the investigation of surfaces. It is based on the photoelectric effect where incident photons with typical energies of some tens to many thousands of eV are absorbed by an atom with a certain probability, proportional to the absorption cross section, a process that, in turn, leads to the emission of an electron if the incident photon energy exceeds the binding energy of the electron in a core or valence level. Each element has a set of characteristic XPS peaks and can thus be uniquely

identified. Moreover, the so-called chemical shifts within each core level spectrum allow for distinguishing different chemical species of an element (e.g., oxidation states and functional groups). The strong dependence of the probing depth in XPS on the electron kinetic energy allows us to obtain depth-dependent information on the elemental and chemical composition at an interface. Typical probing depths are in the nanometer range. Changes in the work function or potential at the surface can also be detected since these affect the electron kinetic energy in all core levels and valence spectra and can thereby be distinguished from chemical shifts. Moreover, through the measurement of the low kinetic energy cutoff, the absolute value of the work function of the sample can be determined; while this method has been applied in investigations on solid samples, it has yet to be demonstrated for liquids.

As we have pointed out before, for investigations of heterogeneous reactions at aqueous solutions, it is, in most cases, necessary to perform measurements at pressures in the mbar range. The mean free path of electrons in the gas phase at these pressures is strongly reduced due to inelastic scattering by gas molecules. A simple estimate for water vapor shows that, since the density of water vapor at 1 mbar is about 10^{-6} of that of condensed water, the mean free path of electrons is about 10^6 of that in the solution, i.e., is in the mm range. The path length of the electrons through the gas phase thus has to be limited to about an mm (or even less when working at higher pressures), which can be achieved using a differentially pumped aperture between the sample cell and the electrostatic lens system of the electron spectrometer. Typical pressure differentials across these apertures are 10^{-2} to 10^{-4}. Several differential pumping stages are necessary for sample cell pressures in the mbar range to ensure high vacuum conditions and avoid arcing at the electron detector, which is operated at high voltages. These ambient pressure XPS spectrometers are now commercially available and have been installed in many laboratories and synchrotron facilities around the world. For more detailed information on APXPS, we refer the reader to a number of review articles (among them, Refs. 69–75).

The close proximity of the sample surface to the differentially pumped front aperture of the electrostatic lens system of the electron analyzer can disturb the gas flow and local pressures at the sample surface, which needs to be evaluated to ensure that the pressure and flow gradients do not interfere with the experiment. In addition, the distance between the sample surface and the aperture has to be as constant as possible; otherwise, the photoelectron intensity fluctuates strongly due to the exponential dependence of the electron attenuation on the distance that the electrons travel through the gas. Both of these considerations are usually not relevant in experiments on solid samples but pose a serious challenge to experiments on liquids, where slight variations in the surface position on the 0.1 mm scale can not only lead to signal fluctuations but also, in the worst case, to entering of the liquid into the electrostatic lens system through the front aperture, with potentially dire consequences for the components of the lens system, including electrical shorts and corrosion. The preparation of liquid surfaces for XPS and APXPS experiments is thus a challenge in itself.

Before discussing strategies for the preparation of liquid–vapor interfaces for surface-sensitive investigations, we first consider the relevant time scales for reactions at liquid–vapor interfaces, since these often govern the choice of preparation method for a given investigation.

B. Relevant time scales for liquid–vapor interface reactions

Chemical reactions take place over a multitude of time scales from electron transfer and bond-breaking/making events on ultrafast time scales to much slower changes in the conformation of larger molecules. Here, we are interested in the time that it takes to reach a steady-state at the liquid–vapor interface and in the bulk solution upon a change in the gas phase composition, which is relevant for the investigation of heterogeneous reactions at liquid–vapor interfaces.

Let us consider the simple situation of an aerosol droplet with a characteristic diameter d of 10 μm consisting of pure water in the absence of any surfactants. Let us assume that initially, the droplet is in equilibrium with its vapor (i.e., neither growing nor shrinking). The droplet is then suddenly exposed to the atmospheric CO_2 partial pressure of 0.4 mbar. What is the time scale for equilibrating the liquid–vapor interface upon the jump in CO_2 partial pressure, and how long will it take for the bulk to reach a steady-state concentration of CO_2?

Let us first neglect chemical reactions occurring in liquid water. Schwartz and Freiberg[76] and Shi and Seinfeld[77] calculated the characteristic time scale τ_{da} at which the equilibration of the bulk solution proceeds,

$$\tau_{da} = \frac{d^2}{\pi^2 D_{sol}}, \tag{1}$$

with D_{sol} being the diffusion coefficient in the solution, which is 2×10^{-9} m^2/s for our example of CO_2 in water at room temperature.[78] For a 10 μm droplet, this then gives an equilibration time of about 5 ms, which is on the order of the time scales available in droplet train[79,80] and liquid jet experiments (see below).

Since XPS is sensitive only to the interfacial region, the equilibration time for the bulk is not necessarily the most important parameter in these experiments. A characteristic time scale τ_{pp} for the establishment of an equilibrium at the liquid–vapor interface can be calculated, again without accounting for chemical reactions, according to Seinfeld,[81] as

$$\tau_{pp} = D_{sol}\left(\frac{4HRT}{\alpha\bar{v}}\right)^2, \tag{2}$$

with H being Henry's law constant, R being the gas constant, T being the temperature, α being the mass accommodation coefficient, and $\bar{v}$ being the average velocity of the molecules in the gas phase. Using numbers for the CO_2–water system at room temperature, i.e., T = 298 K, H = 3.4×10^{-2} mol l^{-1} atm^{-1},[82,83] $\alpha = 2 \times 10^{-4}$,[3] and $\bar{v}$ = 380 m/s, one arrives at equilibration times for the interface in the μs range, i.e., several orders of magnitude faster than required in bulk solution.

The equilibration timescales derived above, which do not consider chemical reactions, can, however, be much shorter than the time required to reach chemical equilibrium. In the widely studied case of CO_2 dissolution,[84] CO_2 reacts with either H_2O or OH^- (the latter reaction dominates for pH > 8.5) to form carbonate species, which are themselves in an acid–base equilibrium depending on

the pH. The abundance of these different species and equilibration timescales involved in the reactions are governed by the kinetic constants of this reaction network and the composition of the aqueous solution. The equilibrium values and kinetic constants depend on the pH, temperature, and pressure,[85–87] and the equilibrium is also influenced by the presence of other ions and molecules, which affects the activities of the species in the carbonate system. The timescale for equilibration of a closed and homogeneous aqueous carbonate system at room temperature can be estimated[84] to be of the order of minutes, depending on the pH and CO_2 concentrations. For an open system where also gas–liquid exchanges are considered, equilibration can take even longer. Diffusion is also not accounted for in this estimation: for a small system such as the droplet case developed above, we saw that the physical timescale of equilibration driven by gas–liquid exchanges and bulk diffusion is much smaller than the chemical equilibration timescale. On the other hand, for larger systems, Eq. (1) shows that the physical timescale can become much larger than the chemical one. The coupling of the reaction and diffusion is specifically treated in Ref. 84.

The equilibration timescale of the interface taking into account chemical reactions is difficult to estimate, and in fact, the investigation of the relations between the bulk and the surface composition and reactivity represents an excellent example for the application of liquid interface science.

While the physical equilibrium between small gas molecules and the aqueous solution surface is established at short timescales, the situation is different when we consider the presence of surfactants at the interface. Depending on the size of the surfactant molecule, the kinetics of the adsorption of these molecules to the surface from the bulk can be on the scale of many minutes or even hours. This has been shown by Rasing et al.[88] in Langmuir trough measurements for the case of sodium-dodecylnapthalene-sulfonate (SDNS). In these measurements, the SDNS surfactant was dissolved into water and the surface of the trough was disturbed using one of the barriers, driving some of the SDNS molecules into the bulk. After separating the two barriers again, the re-adsorption of SDNS to the water–vapor interface was monitored through surface pressure measurements using the Wilhelmy method, as well as SHG.

The results are shown in Fig. 3. The change in the nonlinear susceptibility χ_m/χ_0 and the surface pressure with time is in good agreement and can be modeled with a Langmuir adsorption isotherm. The data in Fig. 3 show that it takes more than an hour until the surface reaches a steady-state condition.

The examples above demonstrate that the equilibration of the interface proceeds on a wide range of time scales, depending on the species involved. In the following, we discuss some of the approaches for the preparation of liquid–vapor interfaces, which are suitable for XPS and APXPS experiments.

C. Preparation of liquid surfaces for XPS

There are a number of different methods for the preparation of liquid interfaces for XPS experiments. The choice of the appropriate method depends on the goal of the experiment and the thermodynamic conditions, particularly the vapor pressure of the solution at the desired sample temperature, as well as the time scale of the expected reactions. For experiments at pressures above
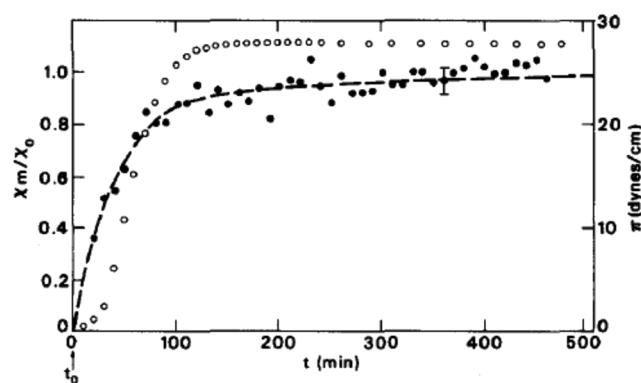
FIG. 3. Equilibration time of a sodium-dodecylnapthalene-sulfonate (SDNS) surfactant layer on water. Open circles show the surface pressure measured by the Wilhelmy method, while full circles display the change in nonlinear susceptibility χ_m/χ_0 obtained from a second-harmonic measurement. The line is a Langmuir-type fit of the surface coverage by SDNS. Reprinted with permission from Rasing et al., J. Chem. Phys. **89**, 3386 (1988). Copyright 1988 AIP Publishing LLC.

10^{-6} mbar, differential pumping between the experimental chamber and analyzer is necessary, and for experiments at pressures above 0.1 mbar, several differential pumping stages and very short path lengths of the electrons inside the experimental cell are required to reduce scattering of electrons by gas molecules, as described in Sec. II A.

Figure 4 shows different preparation methods, most of which have already been used for XPS experiments on liquid–vapor interfaces. The methods in the upper row of Fig. 4 rely on fast flowing liquids that are injected into the vacuum chamber and propagate through it at considerable speed; typical flow rates for jets and droplet trains are of the order of many tens of m/s. If the liquid is caught in a (LN$_2$) cooled trap, the background pressure in the vacuum chamber can be kept in the high vacuum region, for instance, below 10^{-4} mbar for water that is injected at room temperature into the chamber. This enables XPS experiments with very good signal-to-noise ratios and only minimal requirements for additional differential pumping. These methods have been used in the past to investigate the properties of the chemical composition of solutions, where the fast flowing jet or droplet train reduces or even eliminates the commonly encountered problems of beam damage and surface contamination.

The fast flowing jet[52] or droplet[80] setups allow for the change in the solution concentration or pH quickly and seamlessly since the source of the solution is kept outside of the vacuum chamber. Jet and droplet sources can also run in fast mixing modes, where two solutions of different chemical compositions are either mixed just before entering the measurement chamber or mixed inside the chamber (colliding jet/droplet);[89–91] the latter mixing scheme enables measurements from time zero of the mixing event. These methods, in general, provide opportunities for time-resolved studies on the sub-ms to ms time scales for nucleation events and the study of short-lived reaction intermediates. This is especially true for droplet trains, which, in principle, offer a longer time scale for

07 May 2025 10:15:31
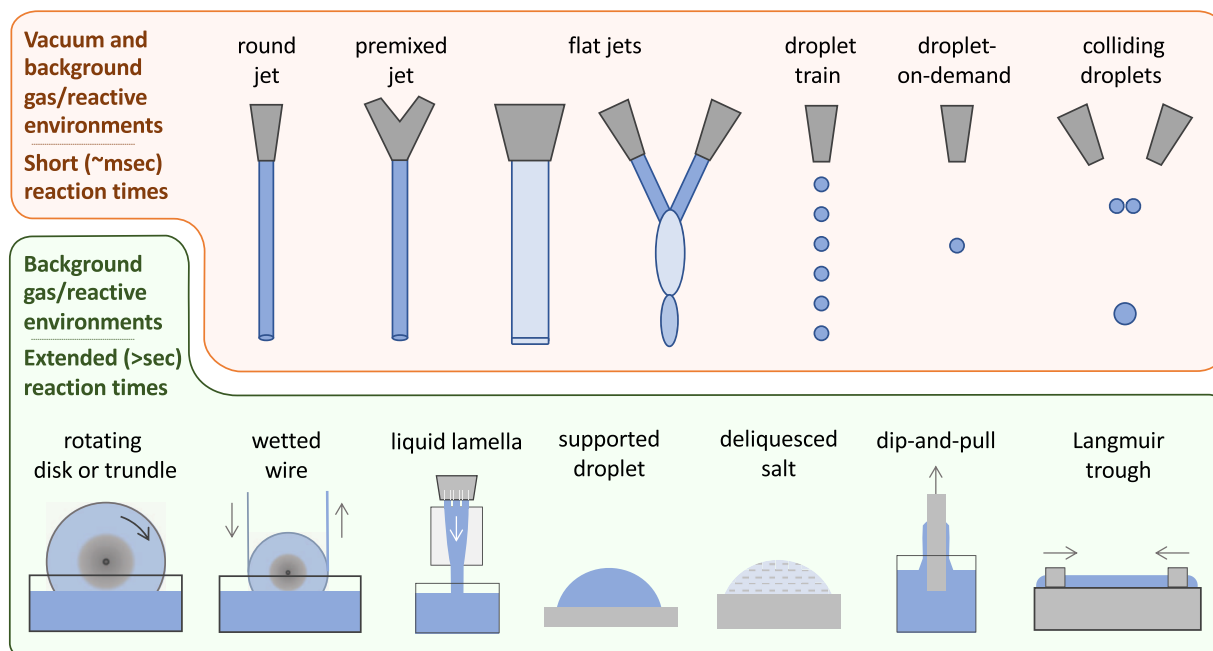
FIG. 4. Preparation of liquid–vapor interfaces inside vacuum chambers. The upper row shows methods based on fast moving jets or droplets that have a very brief interaction time with the surrounding environment before being measured. These methods can be used in a vacuum environment since the liquid reservoir is outside of the vacuum chamber. The bottom row shows preparation methods where the bulk reservoir of the liquid is inside the vacuum chamber and the measurements thus are done in the presence of the equilibrium vapor pressure. These investigations permit longer interaction times between gases and the liquid.

the investigations, since droplets are stable for many centimeters of travel, while jets break up after a few mm due to Rayleigh instabilities. Another feature of fast-flowing jets or droplet trains is the fast evaporation (when used in conjunction with a LN_2 trap), which continually decreases the temperature along the propagation direction, which can be used as an additional parameter in an experiment if the temperature drop can be calibrated, but also, by definition, creates a non-equilibrium at the liquid–vapor interface. Operating a liquid jet under equilibrium vapor pressure conditions nonetheless can and has been done.[92,93]

Many environmental processes occur over longer time intervals than ms and thus require approaches with a longer exposure time between the liquid and the gas phase. Three of those, based on the wetting of a solid substrate in a continuous manner, are shown in the left part of the bottom row of Fig. 4. The rotating disk (or trundle), wetted wire,[67] and liquid lamella[94] methods can be used for intermediate time scales between the fast flowing jets and truly static methods. One point to keep in mind with these approaches is that the reservoir from which the wetting film is created is also in contact with the gas phase, i.e., there is always, most likely, a convolution between the reaction proceeding on the liquid–vapor interface of the wetted surface that is measured by XPS and the reaction between the liquid in the reservoir and the gas atmosphere in the measurement chamber. This also means that the background vapor pressure is set by the equilibrium vapor pressure of the solution in the reservoir, which can be temperature-controlled and thus adjusted over some range down to that of the pressure close to the freezing point. What

makes these methods very attractive, though, is that the liquid surface being measured is constantly refreshed (albeit at a slower rate that in a liquid jet) and thus not very prone to x-ray induced beam damage.

For experiments with (in theory) unlimited reaction times, static liquid surfaces can be prepared in a number of ways, which are depicted in the right part of the bottom row of Fig. 4. Common to all of these methods is that the measurements have to be done in the presence of the equilibrium vapor pressure of the solution; otherwise, the sample will evaporate during the measurements. Hence, these preparation methods require APXPS measurements for most of the solutions of interest, chiefly those of aqueous nature. The most straightforward way is to deposit a droplet of the solution onto a non-reactive substrate, either before evacuation of the chamber or after, in the latter case, e.g., through the use of a pulsed valve. Deposition onto a substrate can also be done through condensation from the vapor phase. This works well for pure solvents, without the addition of a solute, which will not readily evaporate and adsorb on the substrate.

Another straightforward method to investigate saturated aqueous solutions is to deliquesce a salt by adjusting the relative humidity in the measurement cell to the appropriate value, which, for most alkali halides, is between 20% and 90%.[95] The deliquescence point is a triple point in the phase diagram of salts and water vapor, with the solid salt, water vapor, and the saturated solution in equilibrium with each other. While the concentration of the solution is thus well known, the downside of this method is that it does not permit

07 May 2025 10:15:31

the change in the concentration of the solution in a controlled way. Only after all of the solid salt is deliquesced will the concentration of the solution decrease; however, not in an easily adjustable way. One advantage of this method, on the other hand, is that it delivers reliable sensitivity factors for the quantification of relative ionic concentrations through the measurement of the dry salt at low RH before the sample is deliquesced.

The other two methods that allow, in principle, unlimited reaction times are the so-called dip-and-pull (or meniscus) technique and Langmuir troughs. The dip-and-pull method is currently being used for APXPS measurements of solid–liquid interfaces,[96–99] since it allows the preparation of ultra-thin (10 nm–20 nm) solution films on solid substrates by slowly pulling out the substrate from the bulk solution in the presence of the saturation vapor pressure, akin to the procedure used in a Langmuir–Blodgett process. The measurement position is usually many mm (or even cm) above the bulk liquid level in the reservoir, leading to potential limitations in the electronic and ionic transport along the ultra-thin liquid film. Measurements can be done over many hours as long as the liquid film is stable. This method naturally also lends itself to investigations of liquid–vapor interfaces.

The last method discussed here is Langmuir troughs, which have, for many decades, been used for the investigation of the physico–chemical properties of surfactant layers.[100,101] In a Langmuir trough setup, movable barriers allow us to dynamically adjust the packing density of the surfactants and thus to investigate their influence on the structure and chemistry at the liquid–vapor interface. Traditionally, surface-sensitive measurements on thus-prepared surfactant films were performed using optical spectroscopy and hard x-ray based scattering techniques. Some of the authors of this Perspective have recently demonstrated that APXPS is a suitable method for the investigation of the vapor–surfactant/aqueous solution interface and can provide complementary information to optical and scattering methods.[102] We discuss the opportunities for combined APXPS/Langmuir trough measurements in the last part of this Perspective.

Table I lists—to the best of our knowledge—all XPS and APXPS measurements on liquid–vapor interfaces that have been published by the end of May 2020. This table is organized with the preparation method for the liquid–vapor interfaces and lists solvents/solutes as well as background pressures in the experiments. From the table, it is obvious that the overwhelming number of experiments have been performed so far under vacuum conditions using the liquid microjet technique, while investigations under equilibrium vapor pressure conditions are in the minority so far.

After discussing the preparation methods for liquid–vapor interfaces, we now proceed to consider some of the distinct aspects of the analysis of XPS data measured at those interfaces, which can, in some cases, vary with regard to the more commonly obtained data on solid interfaces. In the following, we focus on the basic quantities in an XPS experiment, the signal intensity and electron energy. We start with the non-trivial matter of referencing the electron binding energy scale.

D. Energy referencing

One of the quantities measured in an XPS experiment is the kinetic energy (KE) of the ejected photoelectrons, which for a known

incident photon energy hv reveals the binding energy (BE) of a given element and orbital through the relation BE = $h\nu$ − KE. The core level BE also depends on the local chemical environment (observable through the so-called "chemical shifts")[5,47] and thus serves as a reporter of structural details, including the protonation state in aqueous solutions.[111,121,162] It is, hence, common to present measured photoelectron spectra on the BE scale, even though the measured quantity is the KE. Conversion of KEs to BEs requires a reference point for the BE scale, for instance, the vacuum level or the Fermi edge, or, in some cases, the BE of a certain core level, as will be discussed below. The underlying model for the calculation of the BE values needs to be clearly stated so that the measured KE values can be retrieved for comparison with other measurements.

In most cases, the electron spectrum contains contributions in addition to photoelectrons, for instance, from electrons emitted in second-order relaxation processes (such as Auger decay or other autoionization pathways[47,211–214]) or electrons that have lost discrete or non-discrete fractions of their initial KE through inelastic scattering. Presenting those contributions on the same BE scale is rather meaningless, although commonly accepted within the community; the correct presentation is the measured KE, which, however, is inconvenient when addressing orbital energies. For the sake of completeness, we would like to mention that further complications arise when the core level photoemission spectra are measured near the ionization threshold, the case in which the direct photoelectron and the Auger electron exchange energy via Coulomb interaction with the remaining 1+ and subsequently 2+ charged (final state) ionic species. This so-called post collision interaction (PCI) can be detected as a distortion and shift of both direct and secondary electron peaks.[215–217] For water and aqueous solutions, PCI studies have not yet been reported though.

Another important issue regarding measured electron energies from water or aqueous solutions is the determination of the *absolute* value of a given BE, which requires a robust reference point for the energy scale. Neat water is electrically non-conductive (water can be regarded as a wide-bandgap semiconductor[218]), whereas electric conductivity in the case of dispersed ions can be large. Hence, for neat water as well as in poorly conductive aqueous solutions, the KE of the measured photoelectrons depends on a number of charging effects of the liquid surface (including electrokinetic charging in the case of fast flowing liquid samples and radiation-induced charging[219]), which are typically difficult to quantify experimentally.

In general, the use of gas phase vapor peaks as the internal binding energy reference requires a careful evaluation of the experimental conditions. The vacuum level of the gas phase is tied to that of the nearest surfaces, here chiefly the liquid–vapor interface (in APXPS measurements also, the front aperture of the differentially pumped electrostatic lens system). Any change in the position of the vacuum level of the interface, be it through streaming potentials at the nozzle of liquid jet apertures, through partial orientation of dipoles at the interface, or the preferential presence of certain ions at the interface, will have an influence on the measured gas phase KE. If it can be assured that no electric fields exist between the solution surface and electron detector, solute and solvent peaks can be reasonably well calibrated with reference to the known binding energies of gas-phase water.

07 May 2025 10:15:31

Commonly used references in the literature are the O 1s BE or the $1b_1$ BE of neat liquid water, which, however, have themselves been determined by reference to the respective gas phase water orbitals BEs.[52,109] Furthermore, the BE of these orbitals of water might themselves depend on the presence of solutes and their concentrations and thus not be a meaningful reference. On the contrary, a BE shift of the core and valence levels of water as a function of the solute type and concentration is in itself a quantity that can contain valuable information. This information is lost if the BEs of these peaks are used as an internal reference and set to a certain fixed value.

Different approaches that bypass the gas-phase reference are pursued at present, exploiting the information contained in the low-energy cutoff of the photoelectron spectra. The principal idea has been outlined by Tissot *et al.* for highly saturated salt aqueous solutions deposited on a gold substrate.[208] The analysis here is based on a condensed-matter description, specifically the determination of the Fermi energy and work function. This challenging approach is promising for liquid samples with a high electrical conductivity but suffers from the same limitations in the case of low-conductivity liquids as one encounters in XPS investigations on oxides with high bandgaps.

The ability to measure the work function of the solution surface in vacuum, where possible, will provide valuable additional information in XPS spectra acquired on liquid interfaces, allowing us to quantify the presence and net orientation of molecular surface dipoles.

E. Quantification and depth-profiling

For a better understanding of heterogeneous chemical reactions between aerosols and the surrounding gas phase, quantitative information on the chemical composition of the liquid–vapor interface is essential to aid in the development of atmospheric models. XPS is a quantitative technique particularly suited for this purpose and has been extensively used in solid state surface science. Detailed tutorials on quantification in the solid state exist in textbooks[47,220,221] and will not be reiterated here. Instead, we focus on the most important aspects with regard to liquid interfaces and present some experimental strategies for quantification. A broader question concerns the determination of concentration depth profiles of species across the liquid–vapor interface. This leads us to discuss also the depth sensitivity of XPS, different depth-profiling techniques, and the use of photoelectron angular distributions (PADs) to address this problem.

1. Quantification

The expression for the measured XPS signal intensity for a given peak is usually written in the following form,[117,220] which breaks down the different factors that need to be considered in the quantification of XPS data:

$$I = \alpha \Phi(h\nu) \frac{d\sigma}{d\Omega}(h\nu) T(eKE) \int N(\vec{r}) F(eKE, \vec{r}) dV, \qquad (3)$$

where α is a geometrical factor depending on the illuminated area of the sample and the angular acceptance of the electron analyzer. Φ is

the incident photon flux, which is implicitly assumed to be constant throughout the probed volume in this formula, since the penetration depth of x rays is much larger than the probing depth of XPS. $\frac{d\sigma}{d\Omega}$ is the differential photoemission cross section of the element at the given photon energy, which represents the probability of emission of a photoelectron in the direction of the spectrometer, and thus also depends on the experimental geometry. It can be further broken down as $\frac{d\sigma}{d\Omega} = \sigma f_\sigma(\theta, \phi)$, where σ is the integrated cross section and f_σ is a function describing the electron emission anisotropy. T is the transmission function of the spectrometer, which depends on the kinetic energy of the photoelectron. The last term is the integral over the probed volume of the density N of the considered element at a given point multiplied by an attenuation factor F. Attenuation of the signal is characterized by the mean escape depth (MED) of the electrons, which itself primarily depends on their inelastic mean free paths (IMFPs, see Sec. II E 2). F therefore depends on the photoelectron kinetic energy and the composition and thickness of all the material between the emission point and the entrance of the electron energy analyzer, including the gas phase, which can be relevant for applications at relatively high pressures.

For most practical uses, F is written in the following way:

$$F(z, eKE) = exp\left(-\frac{z}{\lambda(eKE)\cos(\theta)}\right), \qquad (4)$$

where θ is the detection angle of the electrons relative to the surface normal and λ is either directly the IMFP for the considered environment [in the so-called straight-line approximation (SLA) and for a flat surface] or an effective attenuation length (EAL) that also takes into account elastic scattering and geometrical factors (see Secs. II E 2–II E 4).

Liquid–vapor interfaces are not as sharp as solid–gas interfaces, although they exhibit a steep pressure gradient. The broader width of the interfacial region and the often steep gradients in the concentration of ions as a function of depth affect the calculation of the effective attenuation, for which a step-like model for the interface [as in Eq. (4)] is hence not appropriate. Following the work of Ottosson *et al.*,[117] a better description of the attenuation can be achieved by integrating over the density profile at the interface,

$$F'(z, eKE) = exp\left(-\frac{1}{\lambda(eKE)\cos(\theta)} \int_0^z \frac{N(z)}{N_\infty} dz\right), \qquad (5)$$

with N_∞ and $N(z)$ being the total densities of the bulk and at depth z, respectively. λ is assumed here to represent the IMFP for the bulk.

In a strict sense, the attenuation depends not only on the depth-dependent total density but also on the depth-dependent composition of the interface. This is more complicated to take into account and also depends on the *a priori* knowledge of the partial density depth profiles of all different species in the solution, which is usually the unknown quantity that one tries to discern in an XPS experiment.

Quantification, in general, aims at the determination of the depth-dependent density N(z) of an element of a species of interest. If using Eq. (3), the fundamental quantities involved (Φ, σ, D,

IMFPs, etc.) need to be known, or experimental strategies have to be used where these quantities can be eliminated, for instance, by measuring relative chemical compositions. In many cases, approximations are required due to the lack of information on the absolute values of some of the experimental parameters.

Some related specific points that go beyond the problem of quantification are discussed in separate sections afterward but are mentioned here already briefly since they are relevant for the discussion of the quantification:

- Inelastic mean free paths are the fundamental quantities that set the depth sensitivity of XPS, but also one of the biggest unknowns. The relation between the attenuation factor and IMFP depends on the experimental geometry, but also on elastic scattering, which cannot always be neglected. These points are discussed in Sec. II E 2.
- The qualitative and quantitative investigation of surface enhancement/depletion of certain species and the general problem of retrieving the full density profile N(z) of a given species can be addressed using depth-profiling experiments, where the probing depth is varied. Some of these methods are presented in Sec. II E 3.
- The photoemission angular anisotropy f_σ can be cancelled out by using an appropriate experimental geometry, i.e., measuring under the so-called magic angle. However, PADs contain information that can be of interest, and therefore, measuring them when possible is advisable. This is discussed in Sec. II E 4.

We now continue the discussion of the quantification of photoelectron signal intensities. Determining the values for Φ and T [see Eq. (3)] is a matter of calibration. IMFPs and σ are, unfortunately, not fully characterized. An overview of the large uncertainties to which these values are known can be found in Ref. 222 and it is further discussed below in Sec. II E 2. Ionization (also electron detachment) cross sections for solutes and most liquids are unknown, and even the respective gas phase values are rarely available. In practice, calculated atomic data are used.[223,224] It is generally assumed that the atomic cross sections are good approximations as the x-ray absorption cross section for a core shell should be only marginally affected by the chemical environment of the atom for energies far above (>50 eV) the ionization threshold. This assumption can be wrong notably due to interatomic scattering phenomena,[225] which have been shown to persist in liquid media.[140] Therefore, special care has to be taken when comparing XPS intensities from atoms close to heavy (with high electron scattering) atoms (typically chlorinated CCl_x carbon atoms in the above-cited studies) and atoms close to lighter (with low electron scattering) ones (simple hydrogenated CH_x carbons, for example).

Different experimental strategies can be employed to circumvent the need to know some (but rarely all) of the relevant experimental quantities. The relevant quantity in many investigations is the relative abundance of the different elements and chemical species. Thus, one of the most basic experimental strategies is to use a reference signal, for example, the bulk signal of liquid water for aqueous solutions. In this way, only the ratios of the fundamental quantities in Eq. (3) need to be determined. At synchrotron beamlines, experiments can be performed at desirable photon energies to

produce photoelectrons of the same kinetic energy when ionizing different orbitals or different elements. This eliminates the T factor as well as some of the factors arising from the kinetic energy dependence of electron mean free paths, leaving the photon flux and cross sections as the only unknown factors. When experiments are performed at constant photon energy, one can perform calibration experiments on a well-known gas (e.g., CO_2 for the C/O ratio) to obtain a calibration for both the T factor and the photoemission cross section σ. It is also convenient when possible to only compare signal intensities of the same element (e.g., carbon) to eliminate most factors from the equation. For example, although it requires some simplifying assumptions, some authors[128,136] have used ions known to be depleted at the surface as a bulk reference to separate bulk and surface contributions from the signal of other similar species (e.g., succinic acid and its fully deprotonated form[136]).

In some cases, provided that all the above mentioned quantities can be estimated or cancel out, Eq. (3) can be used to obtain the density of a species by a simple calculation. In solid state studies, this is commonly done for layered structures or homogeneous alloys, i.e., when the density can be assumed to be constant over a defined volume. If the density profile has a more complicated form, quantification is more difficult. This is often the case in the liquid state. The density of the solutes varies across the interface, and the size of the interface itself depends on the system under consideration. The interface ends where all species have reached their bulk densities. To give some examples, the interface has a width of ~4 Å (derived from MD simulations[226]) for pure liquid water. It remains similar (again, according to MD simulations) in a solution of succinic acid,[136] as the enhancement of succinic acid at the surface remains confined within 4 Å and coincides with the water interface. On the other hand, Brown et al.[114] estimated that the interface for NO_3^-/NO_2^- aqueous solutions extends up to 30 Å.

Some possible solute density profiles are illustrated in Fig. 5(a). In this figure, the black line is the solvent density, and the z = 0 reference is chosen to be the point where the solvent density is half of its bulk value, which is the most common choice for the Gibbs dividing surface. The colored lines in Fig. 5(a) show possible density profiles for four different solute species, which show enhanced concentrations either at (solutes A, B, and D) or below (solute C) the interface. Distinguishing between the four different cases by just using XPS data is difficult, even when using depth-profiling techniques. Measurements of PADs can actually help in some cases to make this distinction,[166] as mentioned in Sec. II E 4.

Figure 5(b) shows some useful models for the analysis of the interface depth profile structure. One simplifying assumption is to consider the interface as infinitely sharp. Such a model is sketched on the left of Fig. 5(b). In this case, the surface signal is considered to be unattenuated and the bulk signal is not affected by the surface. The XPS signal is then

$$I \propto \Sigma + N_{bulk}\Lambda, \qquad (6)$$

where Σ is the surface concentration of the species and Λ is the mean escape depth, characterizing the probed volume (see Sec. II E 2). One can go a step further and assign a finite thickness to the interface and assume a constant density throughout this layer. This model is sketched in the middle of Fig. 5(b). These simple models have been

07 May 2025 10:15:31
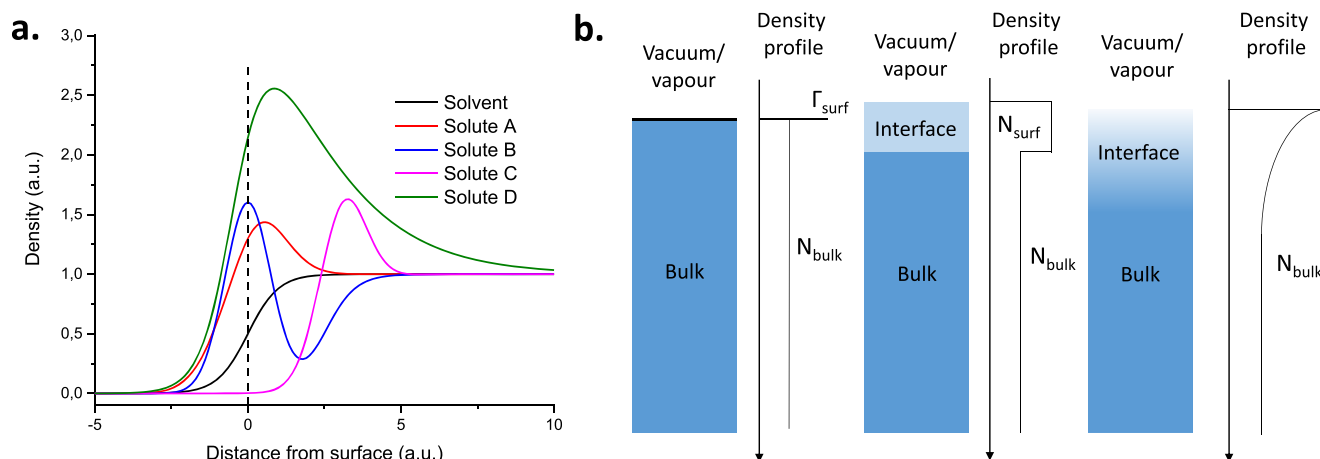
FIG. 5. (a) Some examples of possible density profiles of solutes at the liquid–vapour interface. (b) Some models of density profiles that can be used for analytical quantification. In the first one, the interface is infinitely sharp, while in the second one, it assumes a box shape. In the third one, the density profile is assumed to exponentially decrease from z = 0 to the bulk value.

extensively used to compare the surface behavior of different surfactant molecules and also to connect XPS measurements to the macroscopic measurement of surface tension,[134,136,146,148] which is one of the most common methods of characterization of liquid–vapor interfaces. From concentration-dependent surface tension measurements, one can derive (using thermodynamic considerations) the surface excess of a species. The surface excess describes the enhancement or depletion of a given species at the interface. Ottosson et al.[121] showed a discrepancy in the comparison between the surface excess measured through surface tension and the XPS signal using the infinitely sharp interface model, which shows the influence of the finite extent of the interface.

In some cases,[145,147] quantification using Eq. (3) is not necessary to obtain the surface concentration. For species that have a sufficiently high solubility, concentration-dependent measurements yield Langmuir isotherms for surface adsorption, where the surfactant signal saturates at a given concentration that corresponds to a monolayer, thus providing an intrinsic calibration point, which can be used for all measurements under sub-saturation conditions.

The above considerations apply well to the study of surfactant molecules, particularly neutral surfactants, which tend to adsorb at the surface forming a single layer. Another broad theme of XPS studies of liquid–vapor interfaces is the investigation of the behavior of ions at the interface. Here, the problem is complicated by the formation of an electric double layer at the surface, leading to a more complex depth distribution of the solutes, with an interface depth that can span many nanometers. For instance, in the case of mixed NO_3^-/NO_2^- aqueous solutions mentioned above,[114] a characteristic length (30 Å) of the interface was estimated by using a model that assumes an exponential decay of concentration of the solutes with the depth below the interface. This model is sketched at the right of Fig. 5(b). Studies of ion distributions often require the input from MD simulations and the use of depth-profiling techniques.[117] This

is discussed in Sec. II E 3 below and also more extensively covered in previous reviews such as that by Ammann et al.[66]

2. Inelastic mean free path, effective attenuation length, and depth sensitivity

The inelastic mean free path of the electrons determines the depth sensitivity of an XPS experiment. Even a rough estimate of the probing depth into solution often requires the knowledge of the IMFP (or of the related effective attenuation length; see below). There is a "universal" curve for inelastic mean free paths as a function of electron energy in the sense that all materials (solids, at least) seem to exhibit a curve of similar shape and absolute scale, but only within a factor of 3–5. Therefore, material-specific IMFPs need to be considered.

For solids, an intense effort over decades has been dedicated to determine precise values of the IMFP and to reconcile the scatter of early data. As a result, a consensus has emerged for most common materials and extensive databases exist, such as the NIST database.[227] Such cannot be said for liquids, for which the experimental determination of IMFPs is particularly challenging. Whereas the IMFP for solids can be experimentally determined in a straightforward manner through the measurement of the attenuation of the electron signal from a substrate by an overlayer of the material of interest, whose thickness is independently determined, this method is difficult to apply to liquid samples. While liquid water has been systematically studied, a clear consensus on the IMFP values has not yet been reached. IMFPs for water have been extrapolated from values derived for amorphous ice,[228] calculated using the optical loss function by different algorithms,[229,230] or experimentally derived using photoemission from aqueous solutions.[117,133,139] A recent paper[222] compared the results of Monte Carlo simulations using the differential elastic and inelastic scattering cross sections of water ice to the experimental photoemission results cited above

07 May 2025 10:15:31

and concluded that there is no discrepancy within the uncertainties. This paper therefore suggests at the present stage that the amorphous ice data should be used. Nonetheless, a factor of ~2 of uncertainty remains and the different experimental results are not entirely reconciled (see Fig. 6). The determination of precise IMFPs is an important prerequisite for studies of reactions at the liquid–vapor interface.

A further difficulty is that the precise determination of the IMFP curve for pure liquid water, although it would be an important achievement, is not sufficient: the IMFP will also depend on the solution composition. A comparison of pure liquid water and a 1M NaI solution was made by Olivieri *et al.*[226] using the SESSA software,[231] which uses IMFPs calculated from a semi-empirical formula based on NIST data. They find a difference in IMFP of up to 30% between the two solutions due to the presence of strongly scattering I⁻ anions. Calculations made using SESSA only consider elemental atomic mixtures, and therefore, it remains an open question whether the difference in the electronic structure between such a simple atomic mixture and actual molecules and ions in solution significantly affects IMFPs as well.

The concept of the IMFP by definition neglects elastic scattering and uses the straight-line approximation (SLA), where the attenuation is exponential and the characteristic attenuation length is exactly λ. Elastic scattering leads to deviations from a straight-line trajectory and thus increases the effective distance traveled through the medium (see Fig. 7). Strictly speaking, when elastic scattering is taken into account, the attenuation of the electron signal is no longer described by an exponential dependence on the path length. Elastic scattering is not easily amenable to an exact analytical treatment like inelastic scattering is. However, in practice, approximating the attenuation to an exponential function leads to reasonable results. One can define[117] an effective attenuation length (EAL) λ' as the
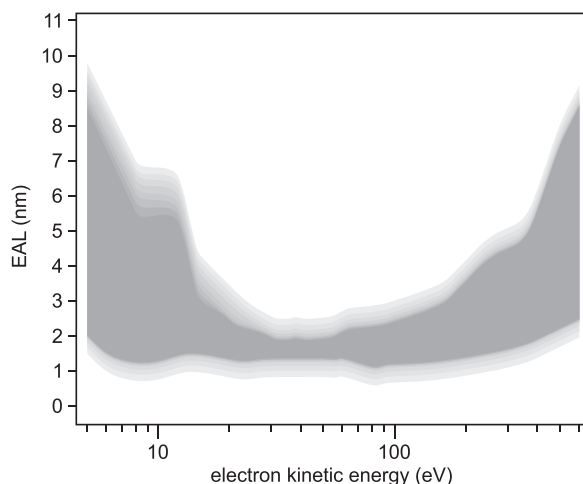
FIG. 6. Illustration of the effective attenuation length (EAL) in water. The shaded area includes experimental values determined from the liquid and gas phase signal contributions in liquid jet core level spectra (detailed description in Refs. 139 and 222) as well as predictions using the scattering cross section of amorphous ice.[228] Adapted from Ref. 222. Experimental data include the results of Refs. 133 and 139.
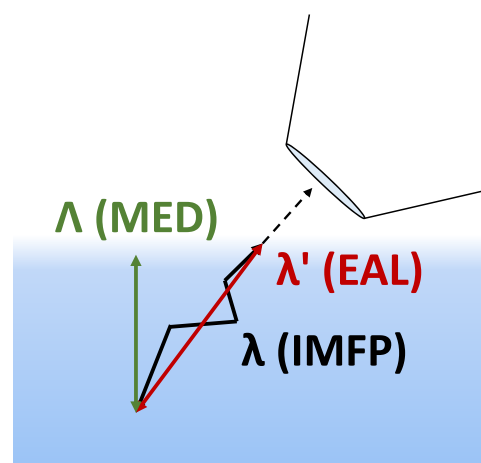
FIG. 7. Illustration of the qualitative differences between inelastic mean free path (IMFP), effective attenuation length (EAL), and mean escape depth (MED).

distance from the emission point for which the initial electron signal is reduced by a factor of 1/e and use this quantity instead of the IMFP. The qualitative difference between EAL and IMFP is illustrated in Fig. 7. The relation between EAL and IMFP depends on the electron kinetic energy and material but also emission angle θ and depth and is therefore complex. However, for $\theta < 60°$, the factor between EAL and IMFP remains mostly constant.[220] For low-Z materials and kinetic energies above 100 eV, the EAL is typically 15%–30% shorter than the IMFP.[52,220] The advantage of the EAL is that it is most often the quantity that is actually of interest for experiments and the one that is measurable by experiments. The experimental studies cited above all measure the EAL, while experimentally determining IMFPs will likely remain elusive. Consequently, the NIST database,[227] for example, compiles EAL values.

Another related quantity is the mean escape depth (MED) of an XPS experiment. For a flat surface and normal detection, the MED coincides with the EAL. However, the MED also depends on experimental geometry. For a flat surface and a detection at an angle θ relative to the surface normal, we have

$$\Lambda = \lambda' \cos(\theta), \qquad (7)$$

where Λ is the MED and λ' is the EAL. This equation is not strictly true for $\theta > 60°$, as the EAL then depends also on the emission angle and the expression becomes more complicated.

Flat surfaces are the most suitable but also—in the case of liquids—experimentally more challenging sample geometry for depth-dependent measurements using XPS. These can be carried out either by varying the detection angle or the electron kinetic energy of the emitted photo electrons. However, the most commonly used technique for the preparation of liquid–vapor interfaces is currently the cylindrical liquid microjet, with consequences for the determination of the mean escape depth of the electrons.
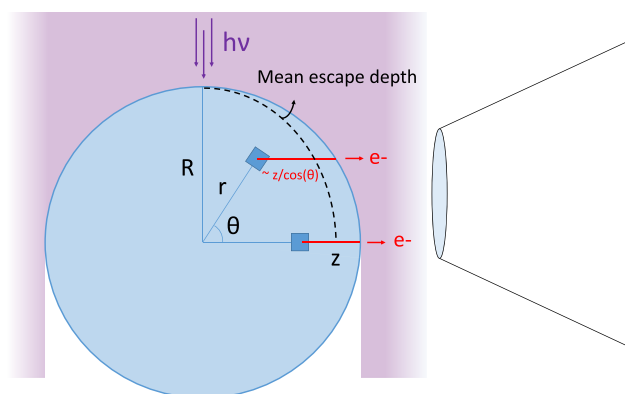
For a cylindrical surface, the angle between the surface normal and the direction of electron detection varies continuously along the circumference (see Fig. 8). Let the radius of the liquid jet be R. For an infinitesimal volume at distance r from the center of the jet and distance z from the surface (i.e., $r + z = R$) along the direction of electron detection, the MED is equal to the EAL (λ') and the signal attenuation is thus $\exp(-z/\lambda')$. For a similar sample volume at angle θ from the electron detection direction and the same distance r from the cylinder surface (see Fig. 8), the projected distance to the jet surface in the direction of the electron detection is then $z/\cos(\theta)$, taking into account that $\lambda' \ll R$ and thus $r \sim R$. It follows that the signal attenuation from this volume is proportional to $\exp(-z/(\cos(\theta)\lambda'))$.

Consider now a geometry (illustrated in Fig. 8) where the x-ray beam is incident at 90° from the direction of electron detection and illuminates the whole jet so that a quarter of the cylinder actually contributes to the signal. In this case, the average mean escape depth is

$$\Lambda_{avg}(E_{kin}) = \frac{2}{\pi}\lambda' \approx 0.63\lambda'. \tag{8}$$

The average mean escape depth for non-flat geometries therefore varies on a case by case basis. For a cylindrical geometry similar to the previously considered one but with a 45° angle between incident beam and detection, one would obtain $\Lambda_{avg} = \frac{2\sqrt{2}}{\pi}\lambda' \approx 0.9\lambda'$. For a spherical geometry (relevant for a droplet train experiment), assuming again an x-ray beam illuminating the whole sphere with an incidence at 90° from the detection, the average mean escape depth would be $\Lambda_{avg} = \frac{4}{\pi^2}\lambda' \approx 0.41\lambda'$. This has consequences in terms of quantification, as Λ is the factor that appears in the attenuation factor in the end.

A more complete comparison of the flat surface and cylindrical surface geometries has been made[232] using the SESSA software (see above), which accounts for elastic scattering, finite acceptance angle, and other parameters. The difference found in escape depth between the two situations is actually smaller than the

FIG. 8. Schematic of a common experimental geometry for a cylindrical liquid jet. The mean escape depth of electrons depends on the angle θ and therefore varies across the jet surface.

37% derived above. The consequences on the XPS signals of ions for a NaI aqueous solution are also evaluated. In a NaI solution, I^- ions are enhanced at the surface by a factor of more than 2 and located slightly closer to the surface than Na^+ ions, which exhibit a lower surface enrichment. The differences for the two geometries in the computed Na/I XPS signal ratio even for the most surface-sensitive photoelectron kinetic energy in this simulation (65 eV) is a few percent, which is almost negligible considering the uncertainties in XPS experiments.

3. Depth-profiling

To obtain more information on the surface vs bulk composition of the solution, one can use depth-profiling techniques that rely on varying the mean escape depth of the electrons, as shown above. The MED Λ equals $\lambda' \cos(\theta)$, and therefore, depth-profiling can be performed by changing the kinetic energy of the photoelectrons (changing λ') or by changing the electron take-off angle relative to the surface (changing θ). Synchrotron-based experiments,[126,202,203] for example, often use photon energies resulting in low (60 eV– 100 eV) and high (600 and more eV) photoelectron KE to make surface and bulk-sensitive measurements, respectively. Comparison between signal intensity ratios at these different kinetic energies gives qualitative information on the surface enhancement or depletion of the species. Note that in some cases (see Sec. III A below), probing into different depths also reveals apparent binding energy shifts associated with different solvation configurations of the solutes.

The most widely studied systems involve aqueous alkali halide solutions (see Table I). Depth-profiling has been used to investigate the specific enhancement of the larger halide anions at the surface.[117,202] However, these studies have often relied on—and have, in fact, been preceded by[233]—molecular dynamics simulations to predict the density profiles of the ions near the surface. An example is shown in Fig. 9(a), which represents the computed density profiles of O, K, and I near the interface of an aqueous KI solution, taken from Ref. 226. Both ions exhibit surface enhancement, but their densities peak at different locations: I^- ions accumulate at the very surface, where the water density decreases, and are slightly depleted lower into the interface, where K^+ ions are enhanced, forming an electric double layer. Such a structure would be difficult to infer using only XPS measurements. The *a priori* density profiles computed by MD simulations can then be connected to the results of depth profiling experiments. This can be done using Eq. (3) to calculate predicted XPS intensities from the computed density profiles, provided that the relevant IMFPs and other factors are known. Another approach is to make use of the SESSA algorithms.[163,226] In this case, the computed density profile is converted into a layer model as the input for the SESSA calculations, which computes directly the expected XPS intensities.

Retrieving more quantitative information about the depth distribution of the solvent and solute species is difficult because the experimental depth resolution is insufficient to resolve the details of the interfacial distribution, as revealed from MD simulations. Indeed, the lowest achievable probing depth in XPS is still of the order of 1 nm, while the interface can be as narrow as 4 Å, as discussed before. In the absence of MD simulations or other *a priori* knowledge on the density profiles, a situation of the type of a KI
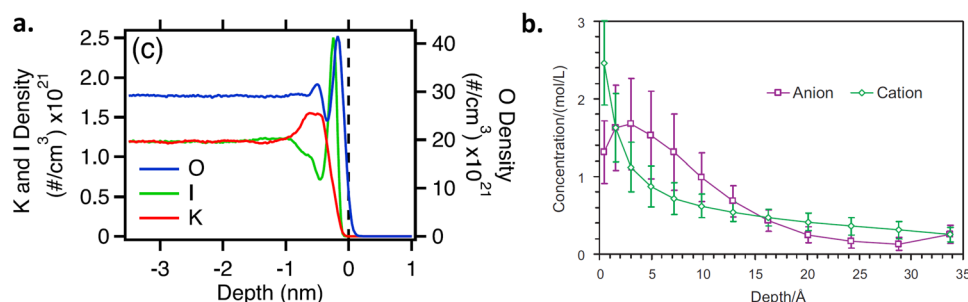
FIG. 9. (a) Molecular dynamics simulation of the density profiles of oxygen, I⁻, and K⁺ at the interface of a 2 M KI aqueous solution. Adapted with permission from Olivieri *et al.*, J. Chem. Phys. **144**, 154704 (2016). Copyright 2016 AIP Publishing LLC. (b) Experimentally determined interface concentration profile of TBA⁺ cation and I⁻ anions of 0.2M TBAI in formamide. Adapted with permission from C. Wang and H. Morgner, Appl. Surf. Sci. **257**, 2291 (2011). Copyright 2011 with permission from Elsevier.

solution described in Fig. 9(a), where two different solutes have a peak in their density profiles at two different locations near the interface, is not easy to discriminate from a situation where the two species peak at the same location. Lewis *et al.*[166] have shown that in such a situation, photoelectron angular distributions (PADs) can be a discriminating tool. This example will be discussed in Sec. II E 4.

In theory, it is possible to retrieve the density profile of a solute from an XPS depth-profiling experiment. Let us rewrite Eq. (3) in the following way:

$$I(\Lambda) = A \int_0^\infty N(z) \exp\left(-\frac{z}{\Lambda}\right) dz. \quad (9)$$

What Eq. (9) shows is that the depth-profiling intensity $I(\Lambda)$ is the Laplace transform of the density profile $N(z)$. One could thus, in principle, obtain the density profile by calculating the inverse Laplace transform of $I(\Lambda)$. This approach is unfortunately complicated by the sensitivity of the inverse Laplace transform to the necessarily limited number of experimental points and the large experimental uncertainties associated.[42] Nonetheless, approaches have been developed to extract $N(z)$ from $I(\Lambda)$ in a reasonably reliable way.

This possibility was first explored by the Baschenko and co-workers. Depth profiling was performed by variation of the electron take-off angle, first using rotating trundle of different inclinations[182,184] and then using a rotating disk whose normal could be adjusted with respect to the analyzer axis.[187–192,194] In the first paper on this topic,[182] the problem of retrieving density profiles is simplified by assuming an exponential decrease in the surface relative to the bulk value. Under this approximation, it is possible to calculate from the spectra a mean segregation depth of the solute. For tetrabutylammonium (TBAI) in formamide, a value of 15 Å is obtained, which is in agreement with the results of a later study.[94] Subsequent experiments applied the same method to the study of other systems. Of particular interest is the paper of Baschenko *et al.*,[192] where a method developed for the retrieval of density profiles in angle-resolved XPS experiments on solids is applied to liquids. In brief, this method tackles the inverse Laplace transform problem by considering a limited number of layers with constant solute densities. Equation (9) can be re-written as a sum of the signals of each layer and numerically solved for the values of the densities of each layer. The procedure is applied to solutions of potassium octanoate in formamide and ethylene glycol.

This approach was further expanded in the Eschen and co-workers. In a synchrotron-based experiment,[94] the liquid lamella technique is applied to prepare a liquid–vapor interface. Both the photoelectron kinetic energies and the electron takeoff angles are varied to perform depth-profiling on the model system of TBAI in formamide. To retrieve the density profile, a layer model is applied. Here, instead of simply fitting the experimental data, a genetic algorithm is used to find the most suitable density profile.[42,94] The interface extends in this case about 15 Å deep into the solution. Many years later, a series of studies were performed by the same group using a lab-based experiment in conjunction with the rotating disk technique,[195,197,198] with the data analysis carried out using a genetic algorithm to retrieve density profiles for TBAI and TBPBr salts in formamide solutions. An example of the results of these studies is displayed in Fig. 9(b), which shows the reconstructed concentration depth profile of TBA⁺ and I⁻ ions for a solution of TBAI in formamide. The technique was also applied to a more complex solution[199] with two surfactants (POPC and TBABr) in a polar solvent (HPN).

We now turn our attention to a further method that can help in obtaining information on the relative position of the solute and solvent species with respect to the interface.

4. Photoelectron angular distributions

Photoemission angular anisotropy is not only a factor that needs to be taken into account when comparing relative peak intensities, and it also reveals additional information. The photoemission angular anisotropy of a molecule primarily depends on (i) the initial state orbital symmetry, (ii) the intra-molecular potential, (iii) the photoelectron kinetic energy, and (iv) the experimental geometry. In addition, the measured angular distribution in condensed matter will be affected by electron scattering. Refer to the relevant reviews for a more thorough description.[47,234]

For randomly oriented gas-phase molecules, a simple expression of the angular distribution of photoelectrons can be derived. If linearly polarized light is used, we have

$$f_\sigma(\theta) = \frac{1}{4\pi}\left(1 + \frac{\beta(eKE)}{2}(3\cos^2(\theta) - 1)\right), \qquad (10)$$

where f_σ is, as defined above, the differential photoemission cross section normalized to the integrated photoemission cross section and θ is the angle between the polarization vector and the electron ejection angle. β is the so-called anisotropy parameter. It can take a value between -1 and 2, with $\beta = 0$ corresponding to an isotropic distribution.[234] The expression for unpolarized incident light is

$$f_\sigma(\theta) = \frac{1}{4\pi}\left(1 - \frac{\beta(eKE)}{4}(3\cos^2(\theta) - 1)\right), \qquad (11)$$

where θ is now the angle between the propagation direction of the incident light and the electron ejection direction. The resulting PADs for linearly polarized and unpolarized light are plotted in Figs. 10(a) and 10(b), respectively, for a few values of β.

In the absence of any scattering, the theoretical value for an s orbital is a constant value $\beta = 2$ at all photoelectron kinetic energies, while β exhibits a kinetic energy dependence for higher symmetry orbitals. Intramolecular scattering often modifies this theoretical value, especially at low photoelectron KE. For gas-phase water, a value of $\beta = 2$ is indeed measured for photoelectron kinetic energies >100 eV, while progressively lower values are observed at lower energies.[133]

In condensed media, the delocalized nature of valence orbitals is expected to affect PADs significantly and reveal important information.[235] On the other hand, localized core orbitals, which are our focus here, are less affected by intermolecular bonding. Thus, PADs of core level photoelectrons will be mostly affected by elastic scattering and the possible spatial ordering of molecules.

Elastic scattering reduces information about the initial ejection direction of photoelectrons and thus tends to randomize PADs toward isotropy. The degree of elastic scattering depends on the photoelectron kinetic energy on the nature of the condensed media and on the distance traveled by electrons through matter. This

information has so far only been exploited in two studies for the liquid phase, to the best of our knowledge.[133,166] While both of these studies were performed on a cylindrical liquid micro-jet, where information on the orientation of molecules at the surface is considerably smeared out, they already demonstrate how PADs provide additional information about the interfacial region.

The aim of the first measurement of PADs of pure liquid water was to derive information on the IMFP[133] in liquid water. In Fig. 10(c), the PAD measurements of this study are reproduced. They show that for electron energies >250 eV, the measured value for O 1s is $\beta \sim 1.5$, lower than the ideal value of 2 for gas phase water. This implies that measured PADs in the condensed phase do contain information about elastic scattering and thus about the localization and environment of the emitting atom.

In the second experiment,[166] PADs were measured for aqueous solutions of organosulfur compounds (DMSO$_x$; x = 1, 2, 3). In the investigation of an aqueous equimolar mixture of DMSO and DMSO$_2$, considerably different S 2p intensities were observed for the two species. However, the anisotropy parameters for both species were found to be similar. This means that photoelectrons from both species experience a similar degree of elastic scattering, which implies that they are located at a similar depth within the solution, contrary to what may have been expected from the different signal intensities. This is one example how PADs can provide unique information about the depth profile of different species.

The random orientation of molecules in the bulk is not maintained at the surface, and thus, one can expect that molecules at the interface show some degree of orientation. A well-known example is the orientation of amphiphilic molecules (e.g., long-chain alcohols or carboxylic acids) at the surface of aqueous solutions, where the nonpolar hydrocarbon chain points toward the gas phase.[105,128,167] For non-randomly oriented molecules, Eqs. (10) and (11) no longer apply, and the PADs contain information about the orientation. In the two above-cited studies where PADs in the aqueous phase have been measured, the PADs are very well fitted by Eq. (10) and thus do not show signs of non-random molecular orientation. Studies
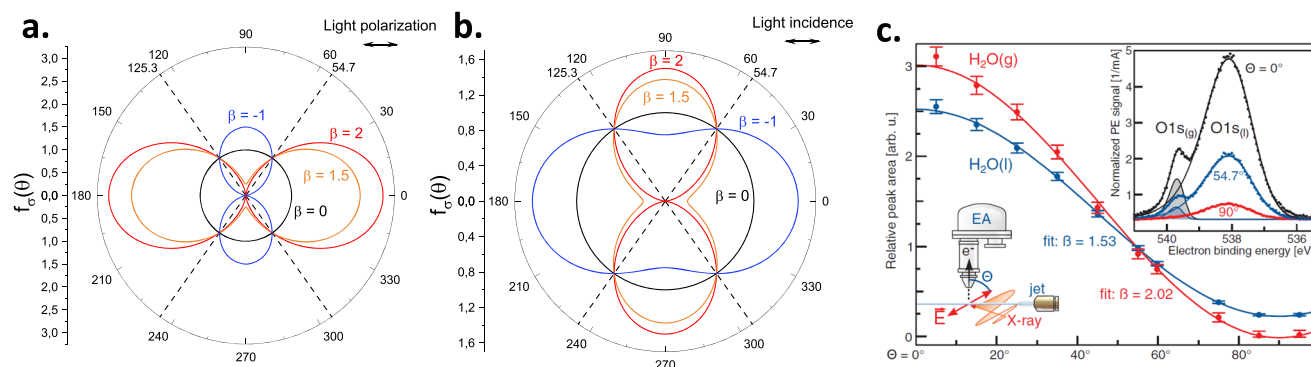
FIG. 10. (a) Representation of the photoelectron angular distribution described by Eq. (10) (linearly polarized light) for different values of β. (b) Representation of the photoelectron angular distribution described by Eq. (11) (unpolarized light) for different values of β. (c) Experimentally measured photoelectron angular distributions for the O 1s orbital of gas-phase and liquid water from a liquid microjet. Adapted with permission from Thürmer *et al.*, Phys. Rev. Lett. **111**, 173005 (2013). Copyright 2013 by the American Physical Society.

making use of flat surface geometries, such as flat jets, Langmuir troughs, or rotating disks will enable us to further explore the effects of preferential molecular orientation on PADs.

In Eq. (3), β appears inside the factor $\frac{d\sigma}{d\Omega}$. When one wishes to compare the relative intensities of peaks, but PADs cannot be measured in the experiment, an experimental geometry can be used to cancel the β dependence. Equations (10) and (11) imply that there are angles for which the β dependence vanishes. These angles, $\theta \sim 54.7°$ $\theta \sim 125.3°$, are the so-called magic angles. This is also clearly visible in Figs. 10(a) and 10(b). Measurements at the magic angle are useful when analyzing peak areas, which are not affected by elastic scattering. This is particularly advantageous when comparing signal intensities arising from ionization of different orbitals.

III. EXAMPLES FOR XPS MEASUREMENTS AT LIQUID–VAPOR INTERFACES

Table I is an attempt at an overview of core level XPS studies on liquid–vapor interfaces since their beginning. It is not our purpose here to discuss all these works in more details. Instead, in this section, a number of selected examples are presented, which focus on the specific topic of reactions at the aqueous solution–vapor interface. These examples were chosen for their relevance in the atmospheric chemistry of aqueous aerosol particles and to provide an overview of the kind of information that is currently obtainable in XPS experiments.

Figure 11 shows an illustration of the discussed examples to emphasize the versatility of XPS for studies of atmospherically relevant interfacial chemistry. The two left panels in Fig. 11 illustrate the different balance of protonation and deprotonation of molecules located at the solution surface compared to the bulk for (a) octanoic acid in the presence of ammonium ions and (b) for a nitric acid (HNO_3) solution. Figure 11(c) shows the capture of carbon dioxide (CO_2) by monoethanolamine (MEA) and (d) shows the oxidation of bromide ions by ozone. These examples are discussed in the following.

A. Protonation and deprotonation of acids

Proton-transfer acid/base reactions are among the most fundamental reactions in aqueous solutions. One may ask whether these reactions proceed differently at the surface. Evidence from surface tension measurements shows that the apparent pK_a of some surface species, such as carboxylic acids,[236] differs from their bulk values, suggesting differences in these basic reactions at the interface. XPS can easily distinguish between the protonated and deprotonated state, as the difference in electron density induces large binding energy shifts of the core levels. It is therefore a powerful technique to address this particular question.

The protonation state of carboxylic acids[121,162] has been investigated in this way. These studies clearly show a surface enhancement of all carboxylic acids. Carboxylates (i.e., the conjugate bases of the acids) are also surface-enhanced for butyrate and longer chains, but less so than the acids due to the lower hydration at the surface. An effective surface pK_a can be derived in this way. The experiments by Werner et al.[162] show that the observed relative abundances of the acid/base conjugates of carboxylic acids and amines at the surface can be entirely explained by the different surface propensities of neutrals and ions without the need of a specific surface protonation or deprotonation reaction.

The same authors have also investigated the acid–base reaction between carboxylic acids and ammonia,[142,167] a reaction believed to be common in atmospheric droplets. Liquid–gas interplay is of importance for this reaction, as the neutral products are both volatiles (for sufficiently small carboxylic acids at least) and can therefore leave the liquid and be transported into the gas phase, shifting the equilibrium toward the neutralization side of the reaction. Öhrwall et al.[142] show that the presence of ammonium significantly increases the surface enhancement of the neutral carboxylic acid relative to the carboxylate. This dramatic enhancement is shown in Fig. 12. The authors suggest that the formation of carboxylate–ammonium bilayers at the interface significantly increases the probability of protonation of the carboxylate into a carboxylic acid. The introduction of ammonium/ammonia to the solution therefore strongly influences the apparent acid–base equilibrium at the solution–gas interface.

Another example of a proton transfer reaction is the dissociation of nitric acid, HNO_3, into NO_3^- and H_3O^+ in water.[123,125] Nitric acid is a prevalent component of atmospheric aerosols, and the extent of nitric acid dissociation at aqueous interfaces is relevant to its role in heterogeneous atmospheric chemistry. The relative amounts of undissociated $HNO_3(aq)$ and dissociated $NO_3^-(aq)$ were identified by their respective N 1s core level peaks in liquid-jet
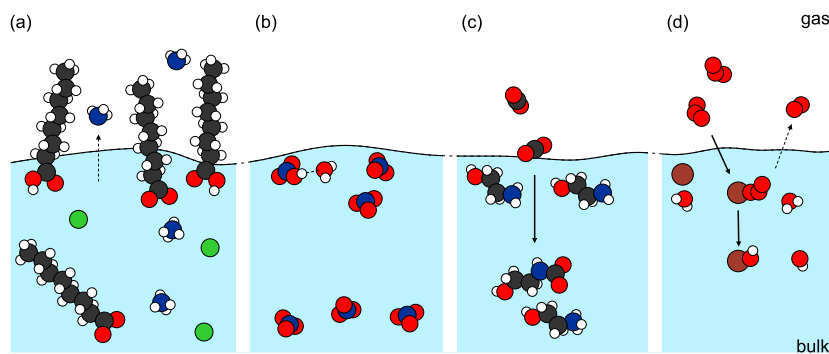
FIG. 11. Schematic illustration of the examples discussed in Sec. III. (a) Octanoic acid protonation/deprotonation in the presence of ammonium. (b) Dissociation of nitric acid at the surface and bulk water. (c) CO_2 capture with monoethanolamine (MEA). (d) Oxidation of bromide with ozone.
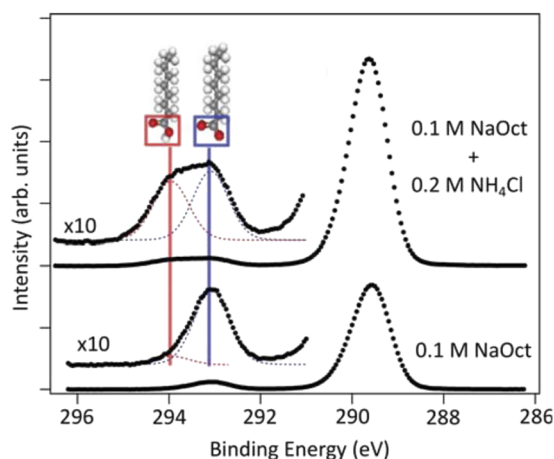
FIG. 12. C 1 s photoelectron spectra of aqueous solutions of 0.1M sodium octanoate and 0.1M sodium octanoate +0.2M NH_4Cl from a liquid jet experiment. The highest peak at 289.5 eV is attributed to CH_x carbons from the hydrocarbon chains, while the two other peaks are attributed to the protonated and deprotonated forms of the COOH group as indicated. The protonated form is significantly increased in the presence of the ammonium salt. Adapted with permission from Öhrwall *et al.*, J. Phys. Chem. B **119**, 4033 (2015). Copyright 2015.

experiments (see Fig. 13), which allowed for a quantitative determination (from analysis of the respective peak areas) of the degree of dissociation at the interface and in the bulk solution as a function of HNO_3 concentration. As shown in Fig. 13, the HNO_3 N 1s BE is slightly smaller and the peak width is slightly larger at the interface than in the bulk, both qualitatively reflecting different solvation configurations of HNO_3 at the solution interface compared to the bulk. A detailed analysis of the BE shifts as a function of HNO_3 concentration is presented in Ref. 125. This is an example where depth-profiling concerns BE as well as relative signal intensity. The main result of the study is that HNO_3 is on average ~20% less dissociated at the solution interface compared to the bulk solution (see the bottom of Fig. 13). Furthermore, dissociation was found not only in the bulk but also at the liquid–vapor interface, a result that is crucial for the understanding of the reaction of interface species with those in the gas phase.

B. CO_2 capture by an aqueous amine-based solution

Amine-based aqueous solutions are solvents commonly used for CO_2 capture. Lewis *et al.*[126] studied aqueous solutions of monoethanolamine (MEA) loaded with CO_2 to better understand the reactions involved and the role of the interface. This is an example of an ex-situ study of a liquid–gas reaction: the MEA solutions were first loaded by bubbling CO_2 gas in the solution under a CO_2 atmosphere and the saturated solutions were then injected into a liquid jet to perform XPS measurements.

CO_2 capture by MEA involves the formation of a carbamate species MEA–COO^- and protonation of another MEA into MEA–H^+. The four species in the solution are therefore the carbamate
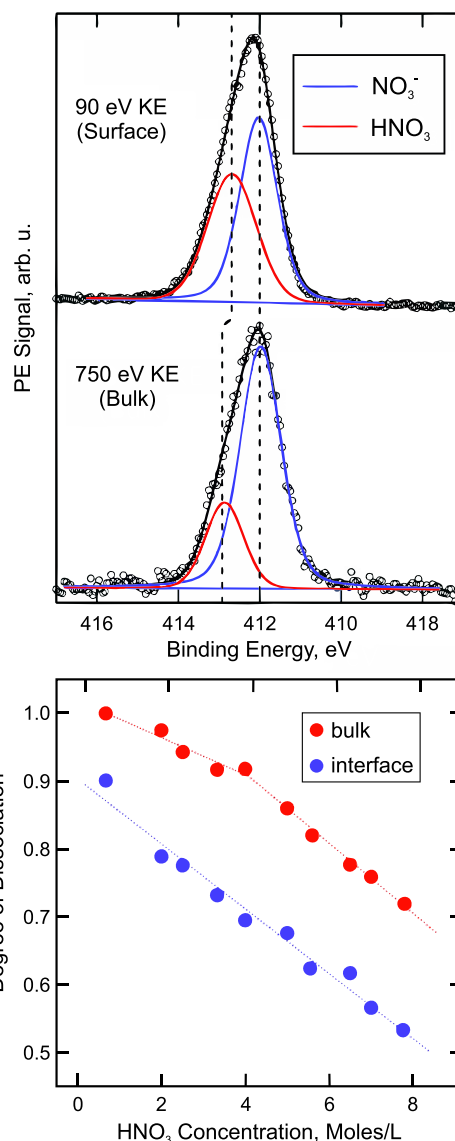
FIG. 13. Top: N 1s photoelectron spectra of a 7.8M nitric acid aqueous solution measured at 500 eV and 1157 eV photon energy, resulting in kinetic energies of emitted electrons as indicated and representing surface and bulk probes, respectively. The two Gaussians highlight the relative signal contribution of molecular HNO_3 and dissociated NO_3^- to the total N 1 s intensity. Bottom: degree of nitric acid dissociation in bulk solutions (red) and at the solution interface (blue) as a function of concentration. The error bars are smaller than the circles and are mainly due to the small HNO_3 signal intensity for the low concentration solutions and also some uncertainties in the solution concentrations. Adapted and reproduced with permission from Lewis *et al.*, J. Phys. Chem. B **115**, 9445 (2011). Copyright 2011 by the American Chemical Society.

and carbamic acid and the protonated and neutral MEA and are quantitatively distinguishable in the C 1s spectra from both the interfacial and bulk aqueous solutions (for a pH near pK_a), as shown in Fig. 14.
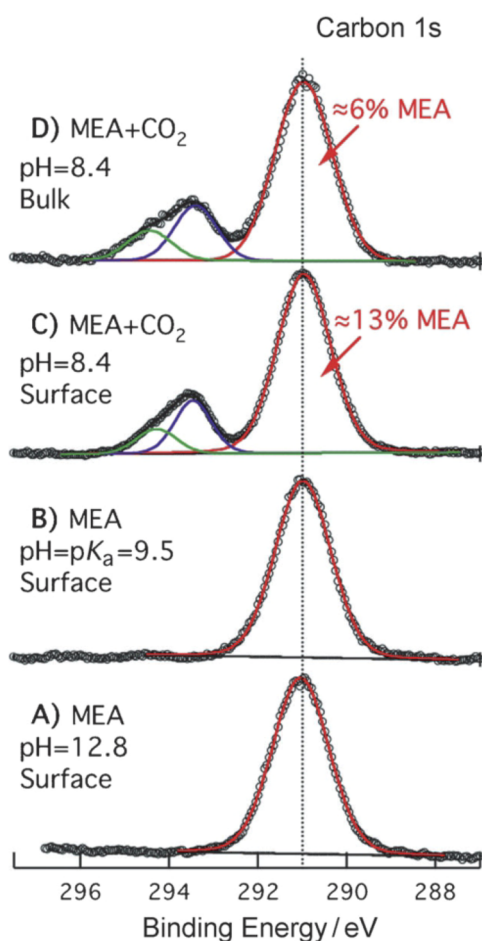
FIG. 14. C 1s spectra of [(a) and (b)] 4.9M MEA and [(c) and (d)] CO_2-treated MEA. In CO_2-treated MEA, peaks due to carbamate (low BE, purple) and carbamic acid (high BE, green) emerge, and the peaks labeled in red show the contribution of neutral MEA. Adapted and reproduced with permission from Lewis *et al.*, Angew. Chem., Int. Ed. **50**, 10178 (2011). Copyright 2011 John Wiley and Sons.

Peak assignments are presented in the figure caption. From the analysis of the respective peak areas in Fig. 14, the pK_a of carbamic acid, which was previously unknown, could be determined to be 8.2. Comparison of surface and bulk-sensitive measurements at different photoelectron kinetic energies allowed the authors to conclude that out of the four species, only MEA is enhanced at the surface. Therefore, during CO_2 uptake by surface MEA, the products of the reaction (carbamate and protonated MEA) tend to move toward the bulk, leaving the surface enriched in MEA and allowing further reactions to take place [depicted in Fig. 11(c)]. This emphasizes the importance of the reaction at the interface, alongside bulk reactions, in this system. It also illustrates how determination of surface propensities through direct methods such as XPS is key to understanding of the details of heterogeneous reactions at the liquid–vapor interface.

C. Bromide oxidation by ozone at the aqueous solution–vapor interface

We now turn our attention to another example of a heterogeneous reaction at the liquid–vapor interface, here an *in situ* experiment. Artiglia *et al.* have studied the formation of a bromide ozonide
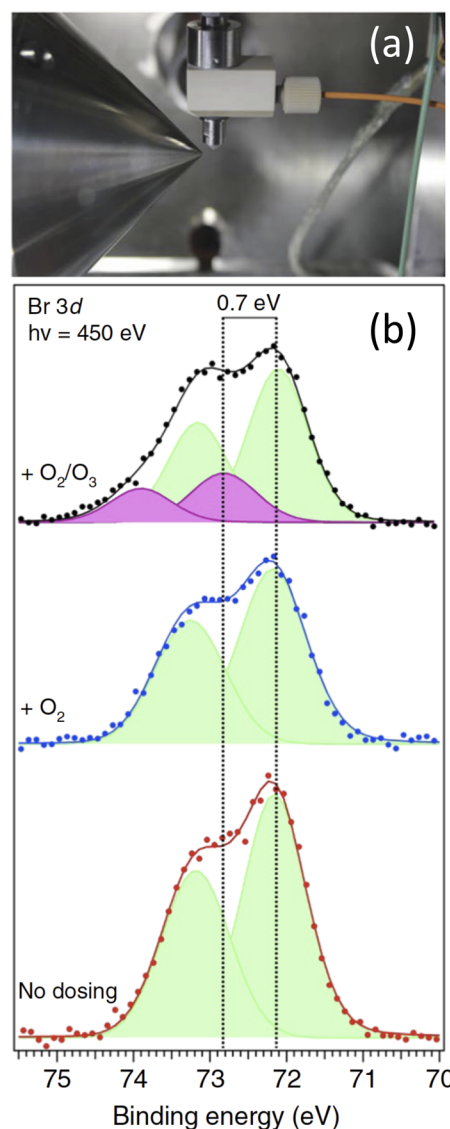
FIG. 15. (a) Liquid microjet setup with the gas dosing system at the Swiss Light Source/Paul Scherrer Institute. (b) Br 3d spectra of an aqueous 0.125M NaBr solution under different gas dosing conditions. Bottom spectrum (red): solution as is. Middle (blue): in the presence of O_2 at 0.25 mbar. Top: in a 1% O_3 in O_2 gas mixture. The light green 3d components are due to the bromine ion, and the magenta components are due to the ozonide that is formed through reaction with ozone. Adapted and reproduced with permission from Artiglia *et al.*, Nat. Commun. **8**, 700 (2017). Copyright 2017 Springer Nature.

($BrOOO^-$) through the reaction of dissolved bromine ions with ozone in a liquid jet experiment.[153]

Figure 15(a) shows the liquid jet in front of the differentially pumped entrance aperture to the electron spectrometer. At the end of the liquid jet, the nozzle is a gas doser, which wraps around the jet filament and thus extends the contact time and collision frequency of the O_2/O_3 reaction mixture. Figure 15(b) displays the Br 3d spectra taken of a 0.125M solution of Br^- under three different conditions: At the bottom without dosing, in the presence of 0.25 mbar O_2 (middle) and in 1% O_3 in 0.25 O_2 mixture (top). While the Br 3d envelope did not change significantly upon the introduction of O_2 compared to vacuum conditions, the small addition of O_3 to the gas phase clearly led to the formation of a new product, signified by the magenta doublet in Fig. 15(b). From a comparison with Br 3d spectra of reference solutions of BrO^- and BrO_3^-, it was concluded that the reaction product formed through the interaction of the bromide solution with ozone was indeed an ozonide. Experiments as a function of kinetic energy and hence probing depth by Artiglia *et al.* revealed that the ozonide complex is most likely surface-bound, which was also supported by MD simulations presented in the same publication.[153]

The investigations described in this and Sec. III B show how, when the reactivity between gas phase species and solution components is high, reaction products can be observed even at the short contact time scales involved in liquid jet experiments. We will expand on this point further in the Prospects section, after we have discussed the use of liquid jet experiments for the observation of short-lived intermediates.

D. Measurement of short-lived species using premixed liquid jets

The last example that we will discuss in this section concerns the use of premixed liquid jets for the investigation of short-lived reaction intermediates. The second vignette from the left in the upper row in Fig. 4 shows the principal idea behind these experiments. The species of interest is generated through the reaction of two precursor solutions right before the jet enters the chamber. Due to the short time that elapses between the generation of the species and the XPS measurement, the decay in the concentration of this species is kept at a manageable level, if the lifetime is of the order of a few milliseconds or more.

This was demonstrated by Lam *et al.* for the case of carbonic acid (H_2CO_3), which is a reaction intermediate when CO_2 is taken up by water. The lifetime of carbonic acid is 26 ms, and the decay products are either dissolved CO_2 or a bicarbonate species (HCO_3^-), which can then further react to a carbonate (CO_3^{2-}). Figure 16(a) shows the C 1s spectra of the pure components; in each case, a 0.5M solution. Carbonic acid was prepared in a small volume right at the exit of the liquid jet by continuously mixing equal amounts of 1M HCl and 1M $NaHCO_3$. The C 1s peaks of the three species are separated by about 1 eV in the order of decreasing charge of the anion, in good agreement with the expected order and magnitude from simple electrostatic considerations.

For an understanding of the interface chemistry between ocean water and air, it is important to determine the relative propensity for the liquid–vapor interface of the different solutes in the water–CO_2 system. To that end, Lam *et al.* prepared 1:1 mixtures of either
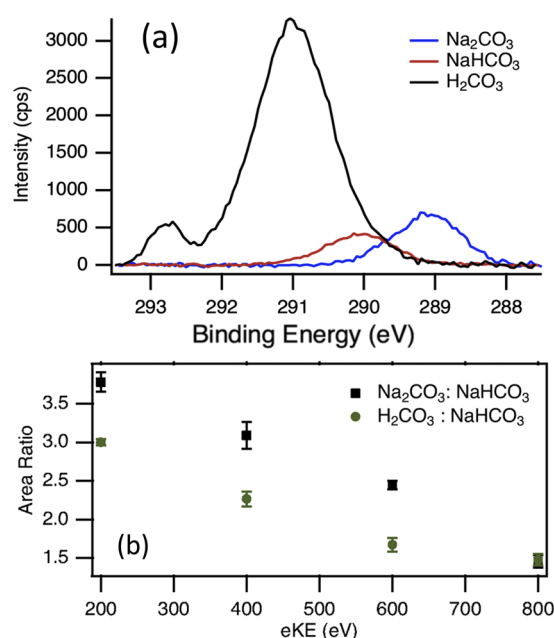
FIG. 16. (a) C 1s spectra of the pure components of the carbonate–bicarbonate–carbonic acid system. The different species can clearly be distinguished by their chemical shifts. (b) Relative intensity of the carbonate vs bicarbonate (black squares) and carbonic acid vs bicarbonate (green circles) peaks as a function of kinetic energy in mixed solutions. For low kinetic energies, i.e., at shallower probing depth, the bicarbonate peak is always weaker, pointing to a depletion of the bicarbonate at the surface relative to the other species. Adapted and reproduced with permission from Lam *et al.*, J. Chem. Phys. **146**, 094703 (2017). Copyright 2017 AIP Publishing LLC.

carbonic acid and bicarbonate or carbonate and bicarbonate (with sodium as the cation in each case) and then recorded C 1s spectra as a function of kinetic energy. Since the peaks of the different species are well-separated, the peak area ratios can be determined in a straightforward way. Figure 16(b) shows the ratios of the peak areas of carbonic acid and carboxyl groups relative to that of the bicarbonate. In the most surface-sensitive measurements at 200 eV KE, both carbonate and carbonic acid are clearly more abundant than bicarbonate, an effect that is less pronounced at a larger probing depth.

This example demonstrates how premixed jets can be used to investigate short-lived intermediates that would otherwise not be accessible in a more static measurement. Besides using a pre-mixed jet, one can also apply two colliding cylindrical jets (of different solutions) to form flat jets or colliding droplets (see Fig. 4).

IV. PROSPECTS

In the last chapter of this Perspective, we will discuss some of the future directions in the area of core level photoelectron spectroscopy on liquid–vapor interfaces. In particular, the development of experimental capabilities for the investigation of heterogeneous

reactions across a wide range of time scales and under realistic conditions of trace gas partial pressures is an important area.[237] We will also discuss some of the experimental challenges that remain and give, where possible, suggestions for how they can be overcome.

A. Time-resolved studies

Atmospheric chemistry studies have identified complex sunlight-induced chemical reactions between aerosols and gaseous species.[9] An important question in modeling such processes is the existence of reactive solute species at the solution (aerosol) surface. In order to understand the reaction kinetics and mechanisms on the microscopic scale, time-resolved experiments using UV/VUV laser pump pulses are required where the temporal evolution of the system is probed by a time-delayed ultrashort x-ray pulse. Relevant time scales in those future experiments will span a large range, covering ultrafast charge transfer (including proton dynamics) and slower reorganization of the solvation shell (e.g., caused by a change in the charge state of the solute), as well as capturing interfacial diffusion processes. Studies will not be limited to mimic exposure to sunlight but include the deliberate formation of reactive interfacial solvated electrons as well as molecular radicals.

1. Ultrafast photoelectron spectroscopy

Ultrafast (sub-picosecond range) photoelectron spectroscopy has been applied to liquids for over a decade by now, starting with studies of the hydrated electron in water.[238–241] The topic was recently reviewed by Suzuki[242] with a focus on aqueous solutions. However, the experiments so far were limited to valence band spectroscopy due to the limited energy range of ultrafast light sources. Synchrotron facilities typically provide x-ray pulses of tens of picosecond widths at about 500 MHz (or ~1 MHz for some special bunch filling). Free electron lasers (FELs) in the x-ray domain on the other hand deliver much shorter pulses but at rather small repetition rates in the kHz range, prohibiting a useful application of XPS to water and aqueous solutions due to the occurrence of space-charge effects as a result of the high number of photons per pulse. Meaningful ultrafast XPS studies of liquids in the soft x-ray regime thus await the next generation of FELs, which will have much higher repetition rates (also afford the application of the required lower single pulse intensity). A viable alternative to FELs are table-top ultrashort pulse EUV and soft x-ray sources (25 eV–600 eV) with a few femtosecond monochromatized pulse durations and ~100 kHz repetition rates, which are currently being developed.[243] The valence band ultrafast PES studies mentioned above make use of such high harmonic generation (HHG) sources operating at reasonably high repetition rates (above 1 kHz) in the extreme ultraviolet (XUV, 30 eV–60 eV).[242,244] Slower dynamics can be explored using picosecond lasers and synchrotron-based x-ray light sources, with associated lasers potentially operating at MHz repetition rates, operating at 25 MHz, with some suitable electronic high-harmonic synchronized to a 500 MHz master frequency demonstrated in Refs. 245 and 246.

A future application of these new light source developments is the study of the liquid–gas interfacial chemistry ideally under conditions that warrant high collision rates between gas-phase species and liquid substrate. The latter would preferentially provide a planar and sufficiently large surface to encourage reactions. This can be achieved by flat (planar) liquid microjets, which can be produced in different ways (see Fig. 4) using suitably structured microchips (offering additional channels to flow or co-flow a gas or gas mixture to increase reaction time)[247] or a pair of colliding cylindrical microjets.[89,90,248] A planar surface has the additional advantage that temporal electronic structure information can be complemented by angle-resolved measurements, and moreover, such geometry is favorable for experiments where molecular beams are scattered off of the liquid surface.

2. Molecular beam scattering on flat jets

A deeper understanding of heterogeneous reactions at liquid–vapor interfaces and the reaction dynamics can be achieved by molecular beam scattering, where translational, rotational, and vibrational degrees of freedom of the gas molecules incident on aqueous solution surfaces can be controlled. Molecular-beam studies have critically contributed to our understanding of gas-phase and gas–solid surface chemistry. Corresponding XPS studies on the surface of highly volatile aqueous solutions have yet to be demonstrated though.

One promising route to successful experiments is to cross a molecular beam with a planar liquid sheet in vacuum (see Fig. 17), generated by colliding two cylindrical microjets. The use of a planar solution surface provides a well-defined scattering geometry that can be modeled in a more straightforward way. In addition, there is a close spatial overlap between the molecular beam diameter and liquid-target surface, which results in a favorable signal-to-noise ratio in the detection of heterogeneous reactions at the liquid–vapor interface.

A major challenge to scattering experiments under elevated pressure conditions are collisions between the incident molecular beam and gas phase molecules, which reduce the number of
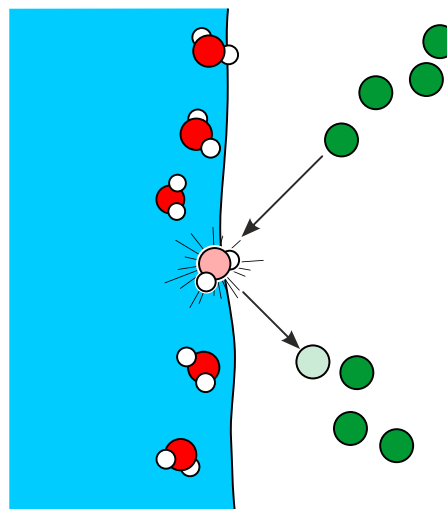

FIG. 17. Schematic drawing of molecular beam scattering on the surface of a flat jet.

scattering events with the liquid under investigation. Molecular beams allow us to probe non-equilibrium chemical reactions, including direct reactions with surface species, or initial physisorption followed by a chemical reaction with subsequent transfer deeper into the solution.

Some of the authors of this Perspective are developing an experiment that will measure XPS spectra under molecular beam on/off conditions, with the goal to detect time-averaged spectroscopic signatures as a function of the colliding gas species and the chemical nature of the liquid interface. One of the open questions is whether these kinds of experiments can—via the detection of chemical shifts—possibly distinguish the solvated species that are formed upon adsorption of gas phase species to the interface from chemically transformed species or reaction products. We note that resonant PES (which is not discussed in the present review) is expected to be a valuable complementary and sensitive spectroscopic tool for probing low-concentration species at the solution interfacial region.[159] Once sufficient know-how for molecular beam scattering off of an aqueous solution surface is established, these studies can be expanded to include photon-induced processes and photochemical reactions.

B. Measurement of heterogeneous liquid–vapor reactions under steady-state conditions

One goal in experiments at liquid–vapor interfaces is to directly monitor the role of surfactants in heterogeneous reactions between trace gases and aqueous interfaces. Some open questions include the formation of reaction intermediates and products at the interface and their fate, i.e., whether these species are incorporated into the bulk of the solution or remain at the liquid–vapor interface as possible participants in subsequent reactions or are desorbed into the gas phase. As was mentioned above, processes involving surfactants often proceed on the minute-to-hour time scale; surface-sensitive investigations on model interfaces thus require the preparation of contamination-free interfaces in a reliable and reproducible manner. This is still an unsolved problem, which is discussed in Sec. IV B 1.

1. Challenges for the preparation of clean static liquid–vapor interfaces

Over the past decades, reliable methods have been developed that enable the preparation of clean solid surfaces for a wide range of materials from metals to oxides to semiconductors.[7] For investigations of the fundamental processes at liquid–vapor interfaces, a similar effort is necessary to establish protocols for the preparation of contamination-free well-controlled static model interfaces. However, applying proven strategies for the preparation of clean solid surfaces to the preparation of liquid interfaces is to a large degree not possible.

This is illustrated in Fig. 18, which shows the two cases side-by-side. Solid surfaces (left panel) are usually prepared under ultra-high vacuum conditions by subsequent cycles of sputtering and annealing, which, over time, depletes the surface and near-surface region of contamination. The slow diffusion of most contaminants (e.g., C, O, N, and S) inside a solid enables measurements of the clean surface over many minutes or hours as long as ultra-high vacuum conditions are maintained.
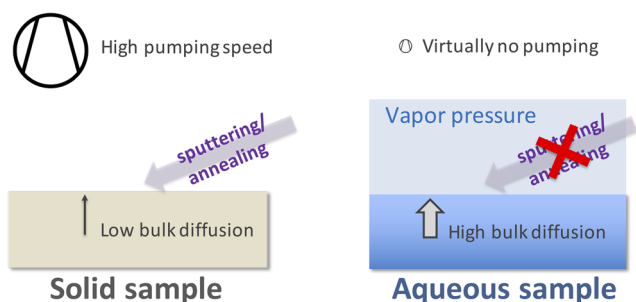
FIG. 18. Left: traditional approach for the reparation of solid surfaces with high purity. Right: these methods are not applicable to liquid/vapor interfaces, which require different approaches.

In the case of static liquids with high vapor pressures, such as aqueous solutions, experiments are either performed in ambient air or inside a vacuum chamber at the equilibrium vapor pressure (see the right panel of Fig. 18). Active pumping on the chamber has to be greatly reduced; otherwise, the sample will evaporate quickly. This precludes the removal of common residual gas contaminants, such as CO or CO_2. Furthermore, a straightforward cleaning method for the surface, akin to sputtering/annealing, is not available, i.e., any residual surface-active contamination in the stock solution from which the sample is prepared can eventually re-adsorb at the liquid–vapor interface.

The combination of a lack of readily available *in situ* cleaning methods for the surface and reduced pumping on the surrounding gas phase pose a serious problem to the preparation of static liquid–vapor interfaces. To illustrate this point, let us assume the example of an aqueous solution at room temperature in the presence of its equilibrium vapor at about 30 mbar. Even if the water vapor would contain background contamination only in the ppm range (i.e., on par with what is available for high purity gases), the partial pressure of the contamination species would still be in the 10^{-5} mbar range. Even if the mass accommodation (or sticking) coefficient of these species is as small as 0.01, a monolayer of contaminants would then form within 10 s, if these species are not dissolved into the bulk.

On the other hand, only small amounts of surface-active contamination in the bulk of the solution will give rise to considerable levels of surface-adsorbed species. For a planar sample, such as in a Langmuir trough (discussed in Sec. IV B 2), the thickness of the solution sample is usually more than a mm. Concentrations of the order of ppm of surface-active species in the solution are sufficient to form a monolayer at the interface if all contaminant molecules adsorb there. The exact coverage of course depends on the propensity of the contamination species for the interface, but these simple estimates illustrate the attention that has to be paid to the preparation of clean solutions and measurement chambers for investigations of well-controlled liquid–vapor interfaces.

2. Multimodal measurements of liquid–vapor interfaces

In the final part of this Perspective, we discuss the development of a new instrument, which is dedicated to the multimodal

07 May 2025 10:15:31
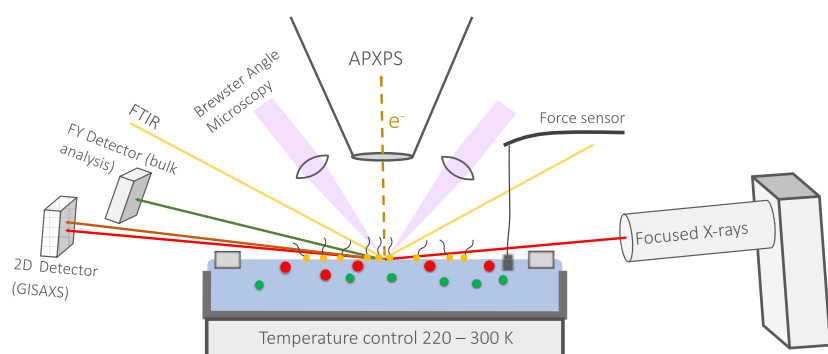
FIG. 19. Schematic layout of a combined APXPS-Langmuir trough instrument that is under construction at the Fritz Haber Institute in Berlin. For details, see the text.

investigation of the heterogeneous chemistry of liquid–vapor interfaces, particularly the role of surfactant layers. This instrument (which will be located at the Fritz Haber Institute) combines several surface-sensitive methods for a more comprehensive characterization of surfactant chemistry at the aqueous solution vapor interface. A schematic of the instrument is shown in Fig. 19. Samples are prepared in a temperature-controlled Langmuir trough, which is located inside a vacuum chamber. The experiments will be done at the equilibrium water vapor pressure and the relevant partial pressures of trace gases in the environment and atmosphere. The main goal of this instrument is investigations of heterogeneous reactions at aqueous solution interfaces involving surfactant layers, which can be prepared in this setup with controlled density.

The properties of the liquid–vapor interface and the bulk of the solution will be probed with a combination of x-ray and optical techniques. The core characterization technique is APXPS (Specs Surface Nanoanalysis, Berlin), which is well-suited for the investigation of surfactant reactions due to the chemical and elemental sensitivity and the ability to probe changes in the work function or dipole moments at the solution interface (see above). A micro-focused laboratory x-ray source (SIGRAY, Concord, CA) provides focused x rays at three different energies, allowing for depth-profiling in the APXPS measurements.

A RAIRS spectrometer (Bruker) is part of the optical characterization. The spectrometer is vacuum-based to minimize the contribution of background gases to the measurements. RAIRS is a complementary technique to APXPS and also provides an important link to past and ongoing experiments on Langmuir trough-prepared liquid–vapor interfaces, where RAIRS is often used as a main characterization technique. In addition Brewster angle microscopy will provide information on the morphology of the surfactant layer. This is important for the correct interpretation of XPS data, since the field of view there is of the order of a few 10 μm, i.e., spatio-temporal changes in the surfactant layer can lead to misinterpretation of the data. In addition, x-ray fluorescence spectroscopy will allow monitoring the elemental composition of the bulk solution and GISAXS provides information on the morphology and ordering of the surfactant layer. An in-vacuum force sensor measures the surface tension as a function of compression of the surfactant layer.

The applicability of all the components of the new instrument to Langmuir trough-based studies has already been shown in the literature or—in the case of APXPS—just recently demonstrated.[102]

It is expected that the simultaneous application of the microscopy and spectroscopy methods under identical experimental conditions will help improve the basic understanding of the complex properties of the volatile and dynamic liquid–vapor interface with high reproducibility and control.

V. CONCLUSIONS

Core level photoelectron spectroscopy of liquid–vapor (particularly aqueous solution–vapor) interfaces has seen a renewed interest in the past 15 years, most notably through the growing availability of liquid microjet experiment stations on synchrotron beamlines throughout the world (see Table I). The field is now ripe for tackling the study of heterogeneous reactions at liquid–vapor interfaces, an important and experimentally challenging task. We have outlined in this Perspective the achievements made so far and attempted to point out what exciting prospects exist and their associated difficulties.

The bulk of the XPS experiments on aqueous solutions has so far focused on the description of the partitioning of ions and small organic molecules to the interface. These studies often exploit the information contained in the photoelectron kinetic energy dependence of the signal intensities (i.e., depth profiling), but also in recent studies through the measurement of the photoelectron angular distributions. Some studies, presented in Sec. III, have already addressed heterogeneous reactions at the liquid–vapor interface.

Efforts have also been made to make XPS of liquid–vapor interfaces a quantitative technique, both in terms of absolute concentration of surface and bulk species and in terms of absolute binding energies. Challenges still lie ahead for both of these points: for the former, they particularly concern the more precise determination of inelastic mean free paths and ionization cross sections in the solution, while for the latter, experiments allowing robust energy referencing need to be designed.

We have pointed out two particular directions in which XPS studies of liquid–vapor interfaces are particularly promising. The first concerns time-resolved experiments, spanning from ultrafast time scales, using new capabilities to generate sub-ps x-ray pulses, to the millisecond time scales accessible in molecular beam scattering experiments. Molecular beam scattering on flat jets will allow

07 May 2025 10:15:31

studies of reactions of gas-phase molecules in controlled states with liquid surfaces. The second direction, at the opposite end of the time scales spectrum, concerns the study of heterogeneous reactions under steady-state conditions. This type of study is equally challenging due to the difficulty of preparing clean static liquid–vapor interfaces. We described the outline for a future instrument that incorporates a Langmuir trough and combines APXPS with several other techniques, with the aim of investigating the heterogeneous chemistry at surfactant-covered liquid–vapor interfaces in a multi-modal manner.

ACKNOWLEDGMENTS

DATA AVAILABILITY

Data sharing is not applicable to this article as no new data were created or analyzed in this study.

REFERENCES

[1] C. L. Sabine, Science **305**, 367 (2004).

[2] I. A. Shiklomanov, in *Water in Crisis*, edited by P. H. Gleick (Oxford University Press, 1993), Chap. 2.

[3] B. J. Finlayson-Pitts and J. N. Pitts, Jr., *Chemistry of the Upper and Lower Atmosphere* (Elsevier, 2000).

[4] N. van Doremalen, T. Bushmaker, D. H. Morris, M. G. Holbrook, A. Gamble, B. N. Williamson, A. Tamin, J. L. Harcourt, N. J. Thornburg, S. I. Gerber, J. O. Lloyd-Smith, E. de Wit, and V. J. Munster, N. Engl. J. Med. **382**, 1564 (2020).

[5] G. Ertl and J. Küppers, *Low Energy Electrons and Surface Chemistry*, 2nd ed. (Wiley-VCH, Weinheim, 1986).

[6] J. W. Niemantsverdriet, *Spectroscopy in Catalysis: An Introduction*, 3rd ed. (Wiley-VCH, Weinheim, Chichester, 2007).

[7] G. A. Somorjai and Y. Li, *Introduction to Surface Chemistry and Catalysis*, 2nd ed. (Wiley, Hoboken, NJ, 2010).

[8] H.-J. Freund, G. Meijer, M. Scheffler, R. Schlögl, and M. Wolf, Angew. Chem., Int. Ed. **50**, 10064 (2011).

[9] B. J. Finlayson-Pitts, Phys. Chem. Chem. Phys. **11**, 7760 (2009).

[10] Z. Peng and J. L. Jimenez, Chem. Soc. Rev. **49**, 2570 (2020).

[11] J. H. Hu, Q. Shi, P. Davidovits, D. R. Worsnop, M. S. Zahniser, and C. E. Kolb, J. Phys. Chem. **99**, 8768 (1995).

[12] A. Heydweiller, Ann. Phys. **338**, 145 (1910).

[13] L. Onsager and N. N. T. Samaras, J. Chem. Phys. **2**, 528 (1934).

[14] L. Wilhelmy, Ann. Phys. **195**, 177 (1863).

[15] C. D. Volpe and S. Siboni, Surf. Innovations **6**, 120 (2017).

[16] D. Hoenig and D. Moebius, J. Phys. Chem. **95**, 4590 (1991).

[17] P. Jungwirth, B. J. Finlayson-Pitts, and D. J. Tobias, Chem. Rev. **106**, 1137 (2006).

[18] S. M. Baumler and H. C. Allen, *Physical Chemistry of Gas–Liquid Interfaces* (Elsevier, 2018), pp. 105–133.

[19] R. A. Dluhy, J. Phys. Chem. **90**, 1373 (1986).

[20] R. Mendelsohn, J. W. Brauner, and A. Gericke, Annu. Rev. Phys. Chem. **46**, 305 (1995).

[21] A. Gericke, J. W. Brauner, R. K. Erukulla, R. Bittman, and R. Mendelsohn, Thin Solid Films **284-285**, 428 (1996).

[22] B. A. Wellen Rudd, A. S. Vidalis, and H. C. Allen, Phys. Chem. Chem. Phys. **20**, 16320 (2018).

[23] R. Raval, Surf. Sci. **331-333**, 1 (1995).

[24] Y. R. Shen and V. Ostroverkhov, Chem. Rev. **106**, 1140 (2006).

[25] S. Gopalakrishnan, D. Liu, H. C. Allen, M. Kuo, and M. J. Shultz, Chem. Rev. **106**, 1155 (2006).

[26] K. B. Eisenthal, Chem. Rev. **96**, 1343 (1996).

[27] M. K. Bera, W. Bu, and A. Uysal, *Physical Chemistry of Gas–Liquid Interfaces* (Elsevier, 2018), pp. 167–194.

[28] W. Bu and M. L. Schlossman, in *Synchrotron Light Sources and Free-Electron Lasers*, edited by E. Jaeschke, S. Khan, J. R. Schneider, and J. B. Hastings (Springer International Publishing, Cham, 2015), pp. 1–33.

[29] S. Myneni, Y. Luo, L. Å. Näslund, M. Cavalleri, L. Ojamäe, H. Ogasawara, A. Pelmenschikov, P. Wernet, P. Väterlein, C. Heske, Z. Hussain, L. G. M. Pettersson, and A. Nilsson, J. Phys.: Condens. Matter **14**, L213 (2002).

[30] K. R. Wilson, M. Cavalleri, B. S. Rude, R. D. Schaller, A. Nilsson, L. G. M. Pettersson, N. Goldman, T. Catalano, J. D. Bozek, and R. J. Saykally, J. Phys.: Condens. Matter **14**, L221 (2002).

[31] G. Hähner, Chem. Soc. Rev. **35**, 1244 (2006).

[32] T. Fransson, Y. Harada, N. Kosugi, N. A. Besley, B. Winter, J. J. Rehr, L. G. M. Pettersson, and A. Nilsson, Chem. Rev. **116**, 7551 (2016).

[33] A. Nilsson, D. Nordlund, I. Waluyo, N. Huang, H. Ogasawara, S. Kaya, U. Bergmann, L.-Å. Näslund, H. Öström, Ph. Wernet, K. J. Andersson, T. Schiros, and L. G. M. Pettersson, J. Electron Spectrosc. Relat. Phenom. **177**, 99 (2010).

[34] J. W. Smith and R. J. Saykally, Chem. Rev. **117**, 13909 (2017).

[35] A. H. England, A. M. Duffin, C. P. Schwartz, J. S. Uejio, D. Prendergast, and R. J. Saykally, Chem. Phys. Lett. **514**, 187 (2011).

[36] J.-H. Guo, Y. Luo, A. Augustsson, S. Kashtanov, J.-E. Rubensson, D. K. Shuh, H. Ågren, and J. Nordgren, Phys. Rev. Lett. **91**, 157401 (2003).

[37] U. Bergmann, P. Wernet, P. Glatzel, M. Cavalleri, L. G. M. Pettersson, A. Nilsson, and S. P. Cramer, Phys. Rev. B **66**, 092107 (2002).

[38] L. Weinhardt, M. Blum, O. Fuchs, A. Benkert, F. Meyer, M. Bär, J. D. Denlinger, W. Yang, F. Reinert, and C. Heske, J. Electron Spectrosc. Relat. Phenom. **188**, 111 (2013).

[39] V. Vaz da Cruz, F. Gel'mukhanov, S. Eckert, M. Iannuzzi, E. Ertan, A. Pietzsch, R. C. Couto, J. Niskanen, M. Fondell, M. Dantz, T. Schmitt, X. Lu, D. McNally, R. M. Jay, V. Kimberg, A. Föhlisch, and M. Odelius, Nat. Commun. **10**, 1013 (2019).

[40] A. Nilsson, T. Tokushima, Y. Horikawa, Y. Harada, M. P. Ljungberg, S. Shin, and L. G. M. Pettersson, J. Electron Spectrosc. Relat. Phenom. **188**, 84 (2013).

[41] G. Andersson and C. Ridings, Chem. Rev. **114**, 8361 (2014).

[42] G. Andersson and H. Morgner, in *Surface and Interface Science*, 1st ed., edited by K. Wandelt (Wiley, 2020), pp. 229–350.

[43] J. A. Faust and G. M. Nathanson, Chem. Soc. Rev. **45**, 3609 (2016).

[44] M. A. Tesa-Serrate, E. J. Smoll, T. K. Minton, and K. G. McKendrick, Annu. Rev. Phys. Chem. **67**, 515 (2016).

[45] S.-C. Park, D. K. Burden, and G. M. Nathanson, Acc. Chem. Res. **42**, 379 (2009).

[46] F. Eschen, H. Morgner, and J. Vogt, J. Electron Spectrosc. Relat. Phenom. **82**, 145 (1996).

[47] S. Hüfner, "Photoelectron spectroscopy," in *Advanced Texts in Physics* (Springer Berlin Heidelberg, Berlin, Heidelberg, 2003).

[48] S. Thürmer, R. Seidel, W. Eberhardt, S. E. Bradforth, and B. Winter, J. Am. Chem. Soc. **133**, 12528 (2011).

[49] R. Seidel, B. Winter, and S. E. Bradforth, Annu. Rev. Phys. Chem. **67**, 283 (2016).

[50] E. W. Castner and J. F. Wishart, J. Chem. Phys. **132**, 120901 (2010).

[51] R. Hayes, G. G. Warr, and R. Atkin, Chem. Rev. **115**, 6357 (2015).

[52] B. Winter and M. Faubel, Chem. Rev. **106**, 1176 (2006).

[53] D. E. Starr, E. K. Wong, D. R. Worsnop, K. R. Wilson, and H. Bluhm, Phys. Chem. Chem. Phys. **10**, 3093 (2008).

07 May 2025 10:15:31

[54] H. Siegbahn and K. Siegbahn, J. Electron Spectrosc. Relat. Phenom. **2**, 319 (1973).

[55] R. S. Weatherup, B. Eren, Y. Hao, H. Bluhm, and M. B. Salmeron, J. Phys. Chem. Lett. **7**, 1622 (2016).

[56] P. Amann, D. Degerman, M.-T. Lee, J. D. Alexander, M. Shipilin, H.-Y. Wang, F. Cavalca, M. Weston, J. Gladh, M. Blom, M. Björkhage, P. Löfgren, C. Schlueter, P. Loemker, K. Ederer, W. Drube, H. Noei, J. Zehetner, H. Wentzel, J. Åhlund, and A. Nilsson, Rev. Sci. Instrum. **90**, 103102 (2019).

[57] Y. Takagi, T. Nakamura, L. Yu, S. Chaveanghong, O. Sekizawa, T. Sakata, T. Uruga, M. Tada, Y. Iwasawa, and T. Yokoyama, Appl. Phys. Express **10**, 076603 (2017).

[58] J. J. Velasco-Velez, V. Pfeifer, M. Hävecker, R. S. Weatherup, R. Arrigo, C.-H. Chuang, E. Stotz, G. Weinberg, M. Salmeron, R. Schlögl, and A. Knop-Gericke, Angew. Chem., Int. Ed. **54**, 14554 (2015).

[59] J. J. Velasco-Vélez, V. Pfeifer, M. Hävecker, R. Wang, A. Centeno, A. Zurutuza, G. Algara-Siller, E. Stotz, K. Skorupska, D. Teschner, P. Kube, P. Braeuninger-Weimer, S. Hofmann, R. Schlögl, and A. Knop-Gericke, Rev. Sci. Instrum. **87**, 053121 (2016).

[60] T. Buttersack, P. E. Mason, R. S. McMullen, T. Martinek, K. Brezina, D. Hein, H. Ali, C. Kolbeck, C. Schewe, S. Malerz, B. Winter, R. Seidel, O. Marsalek, P. Jungwirth, and S. E. Bradforth, J. Am. Chem. Soc. **141**, 1838 (2019).

[61] T. Buttersack, P. E. Mason, P. Jungwirth, H. C. Schewe, B. Winter, R. Seidel, R. S. McMullen, and S. E. Bradforth, Rev. Sci. Instrum. **91**, 043101 (2020).

[62] T. Buttersack, P. E. Mason, R. S. McMullen, H. C. Schewe, T. Martinek, K. Brezina, M. Crhan, A. Gomez, D. Hein, G. Wartner, R. Seidel, H. Ali, S. Thürmer, O. Marsalek, B. Winter, S. E. Bradforth, and P. Jungwirth, Science **368**, 1086 (2020).

[63] M. A. Brown, M. Faubel, and B. Winter, Annu. Rep. Prog. Chem., Sect. C: Phys. Chem. **105**, 174 (2009).

[64] B. Winter, Nucl. Instrum. Methods Phys. Res., Sect. A **601**, 139 (2009).

[65] R. Seidel, S. Thürmer, and B. Winter, J. Phys. Chem. Lett. **2**, 633 (2011).

[66] M. Ammann, L. Artiglia, and T. Bartels-Rausch, *Physical Chemistry of Gas–Liquid Interfaces* (Elsevier, 2018), pp. 135–166.

[67] H. Siegbahn, J. Phys. Chem. **89**, 897 (1985).

[68] M. A. Brown, I. Jordan, A. Beloqui Redondo, A. Kleibert, H. J. Wörner, and J. A. van Bokhoven, Surf. Sci. **610**, 1 (2013).

[69] M. Salmeron and R. Schlögl, Surf. Sci. Rep. **63**, 169 (2008).

[70] C. Arble, M. Jia, and J. T. Newberg, Surf. Sci. Rep. **73**, 37 (2018).

[71] H. Ogasawara, S. Kaya, and A. Nilsson, Top. Catal. **59**, 439 (2016).

[72] B. S. Mun, H. Kondoh, Z. Liu, P. N. Ross, and Z. Hussain, in *Current Trends of Surface Science and Catalysis*, edited by J. Y. Park (Springer, New York, NY, 2014), pp. 197–229.

[73] D. E. Starr, Z. Liu, M. Hävecker, A. Knop-Gericke, and H. Bluhm, Chem. Soc. Rev. **42**, 5833 (2013).

[74] H. Bluhm, J. Electron Spectrosc. Relat. Phenom. **177**, 71 (2010).

[75] L. Trotochaud, A. R. Head, O. Karslıoğlu, L. Kyhl, and H. Bluhm, J. Phys.: Condens. Matter **29**, 053002 (2017).

[76] S. E. Schwartz and J. E. Freiberg, Atmos. Environ. (1967) **15**, 1129 (1981).

[77] B. Shi and J. H. Seinfeld, Atmos. Environ., Part A **25**, 2371 (1991).

[78] S. P. Cadogan, G. C. Maitland, and J. P. M. Trusler, J. Chem. Eng. Data **59**, 519 (2014).

[79] D. R. Worsnop, Q. Shi, J. T. Jayne, C. E. Kolb, E. Swartz, and P. Davidovits, J. Aerosol Sci. **32**, 877 (2001).

[80] D. R. Worsnop, M. S. Zahniser, C. E. Kolb, J. A. Gardner, L. R. Watson, J. M. Van Doren, J. T. Jayne, and P. Davidovits, J. Phys. Chem. **93**, 1159 (1989).

[81] J. H. Seinfeld, *Atmospheric Chemistry and Physics of Air Pollution* (John Wiley & Sons, Inc., New York, 1986).

[82] J. J. Carroll, J. D. Slupsky, and A. E. Mather, J. Phys. Chem. Ref. Data **20**, 1201 (1991).

[83] R. Sander, Atmos. Chem. Phys. **15**, 4399 (2015).

[84] R. E. Zeebe and D. Wolf-Gladrow, *CO_2 in Seawater: Equilibrium, Kinetics, Isotopes*, Elsevier Oceanography Series (Elsevier Science, 2001), Vol. 65.

[85] Z. Duan and R. Sun, Chem. Geol. **193**, 257 (2003).

[86] Z. Duan, R. Sun, C. Zhu, and I.-M. Chou, Mar. Chem. **98**, 131 (2006).

[87] X. Wang, W. Conway, R. Burns, N. McCann, and M. Maeder, J. Phys. Chem. A **114**, 1734 (2010).

[88] T. Rasing, T. Stehlin, Y. R. Shen, M. W. Kim, and P. Valint, J. Chem. Phys. **89**, 3386 (1988).

[89] M. Kubin, M. Guo, M. Ekimova, M. L. Baker, T. Kroll, E. Källman, J. Kern, V. K. Yachandra, J. Yano, E. T. J. Nibbering, M. Lundberg, and P. Wernet, Inorg. Chem. **57**, 5449 (2018).

[90] M. Ekimova, W. Quevedo, M. Faubel, P. Wernet, and E. T. J. Nibbering, Struct. Dyn. **2**, 054301 (2015).

[91] M. I. Jacobs, J. F. Davies, L. Lee, R. D. Davis, F. Houle, and K. R. Wilson, Anal. Chem. **89**, 12511 (2017).

[92] K. A. Perrine, M. H. C. Van Spyk, A. M. Margarella, B. Winter, M. Faubel, H. Bluhm, and J. C. Hemminger, J. Phys. Chem. C **118**, 29378 (2014).

[93] M. A. Brown, M.-T. Lee, A. Kleibert, M. Ammann, and J. B. Giorgi, J. Phys. Chem. C **119**, 4976 (2015).

[94] F. Eschen, M. Heyerhoff, H. Morgner, and J. Vogt, J. Phys.: Condens. Matter **7**, 1961 (1995).

[95] S. T. Martin, Chem. Rev. **100**, 3403 (2000).

[96] M. Favaro, B. Jeong, P. N. Ross, J. Yano, Z. Hussain, Z. Liu, and E. J. Crumlin, Nat. Commun. **7**, 12695 (2016).

[97] S. Axnanda, E. J. Crumlin, B. Mao, S. Rani, R. Chang, P. G. Karlsson, M. O. M. Edwards, M. Lundqvist, R. Moberg, P. Ross, Z. Hussain, and Z. Liu, Sci. Rep. **5**, 9788 (2015).

[98] M. Favaro, F. F. Abdi, E. J. Crumlin, Z. Liu, R. van de Krol, and D. E. Starr, Surfaces **2**, 78 (2019).

[99] O. Karslıoğlu, S. Nemšák, I. Zegkinoglou, A. Shavorskiy, M. Hartl, F. Salmassi, E. M. Gullikson, M. L. Ng, C. Rameshan, B. Rude, D. Bianculli, A. A. Cordones, S. Axnanda, E. J. Crumlin, P. N. Ross, C. M. Schneider, Z. Hussain, Z. Liu, C. S. Fadley, and H. Bluhm, Faraday Discuss. **180**, 35 (2015).

[100] M. S. Aston, Chem. Soc. Rev. **22**, 67 (1993).

[101] H. Möhwald, Rep. Prog. Phys. **56**, 653 (1993).

[102] H. Hoek, T. Gerber, C. Richter, R. Dupuy, R. Rapf, H. Oertel, L. Trotochaud, O. Karslioglu, D. Goodacre, M. Huber, M. Blum, S. Gericke, C. Buechner, F. Borondics, B. Rude, F. Mugele, K. R. Wilson, R. Schlögl, and H. Bluhm, "Compression of a stearic acid surfactant layer on water investigated by ambient pressure XPS" (unpublished).

[103] H. Siegbahn, L. Asplund, P. Kelfve, K. Hamrin, L. Karlsson, and K. Siegbahn, J. Electron Spectrosc. Relat. Phenom. **5**, 1059 (1974).

[104] H. Siegbahn, L. Asplund, P. Kelfve, and K. Siegbahn, J. Electron Spectrosc. Relat. Phenom. **7**, 411 (1975).

[105] B. Winter, R. Weber, P. M. Schmidt, I. V. Hertel, M. Faubel, L. Vrbka, and P. Jungwirth, J. Phys. Chem. B **108**, 14558 (2004).

[106] B. Winter, R. Weber, I. V. Hertel, M. Faubel, L. Vrbka, and P. Jungwirth, Chem. Phys. Lett. **410**, 222 (2005).

[107] D. Nolting, E. F. Aziz, N. Ottosson, M. Faubel, I. V. Hertel, and B. Winter, J. Am. Chem. Soc. **129**, 14068 (2007).

[108] N. Bergersen, R. R. T. Marinho, W. Pokapanich, A. Lindblad, O. Björneholm, L. J. Sæthre, and G. Öhrwall, J. Phys.: Condens. Matter **19**, 326101 (2007).

[109] B. Winter, E. F. Aziz, U. Hergenhahn, M. Faubel, and I. V. Hertel, J. Chem. Phys. **126**, 124504 (2007).

[110] M. A. Brown, R. D'Auria, I.-F. W. Kuo, M. J. Krisch, D. E. Starr, H. Bluhm, D. J. Tobias, and J. C. Hemminger, Phys. Chem. Chem. Phys. **10**, 4778 (2008).

[111] D. Nolting, N. Ottosson, M. Faubel, I. V. Hertel, and B. Winter, J. Am. Chem. Soc. **130**, 8150 (2008).

[112] N. Ottosson, R. Vácha, E. F. Aziz, W. Pokapanich, W. Eberhardt, S. Svensson, G. Öhrwall, P. Jungwirth, O. Björneholm, and B. Winter, J. Chem. Phys. **131**, 124706 (2009).

[113] B. Winter, M. Faubel, R. Vácha, and P. Jungwirth, Chem. Phys. Lett. **474**, 241 (2009).

[114] M. A. Brown, B. Winter, M. Faubel, and J. C. Hemminger, J. Am. Chem. Soc. **131**, 8354 (2009).

[115] N. Ottosson, J. Heyda, E. Wernersson, W. Pokapanich, S. Svensson, B. Winter, G. Öhrwall, P. Jungwirth, and O. Björneholm, Phys. Chem. Chem. Phys. **12**, 10693 (2010).

[116]G. Öhrwall, N. Ottosson, W. Pokapanich, S. Legendre, S. Svensson, and O. Björneholm, J. Phys. Chem. B **114**, 17057 (2010).

[117]N. Ottosson, M. Faubel, S. E. Bradforth, P. Jungwirth, and B. Winter, J. Electron Spectrosc. Relat. Phenom. **177**, 60 (2010).

[118]M. A. Brown, R. Seidel, S. Thürmer, M. Faubel, J. C. Hemminger, J. A. van Bokhoven, B. Winter, and M. Sterrer, Phys. Chem. Chem. Phys. **13**, 12720 (2011).

[119]S. Thürmer, R. Seidel, B. Winter, M. Ončák, and P. Slavíček, J. Phys. Chem. A **115**, 6239 (2011).

[120]N. Ottosson, K. J. Børve, D. Spångberg, H. Bergersen, L. J. Sæthre, M. Faubel, W. Pokapanich, G. Öhrwall, O. Björneholm, and B. Winter, J. Am. Chem. Soc. **133**, 3120 (2011).

[121]N. Ottosson, E. Wernersson, J. Söderström, W. Pokapanich, S. Kaufmann, S. Svensson, I. Persson, G. Öhrwall, and O. Björneholm, Phys. Chem. Chem. Phys. **13**, 12261 (2011).

[122]J. Söderström, N. Ottosson, W. Pokapanich, G. Öhrwall, and O. Björneholm, J. Electron Spectrosc. Relat. Phenom. **184**, 375 (2011).

[123]T. Lewis, B. Winter, A. C. Stern, M. D. Baer, C. J. Mundy, D. J. Tobias, and J. C. Hemminger, J. Phys. Chem. C **115**, 21183 (2011).

[124]K. Nishizawa, N. Kurahashi, K. Sekiguchi, T. Mizuno, Y. Ogi, T. Horio, M. Oura, N. Kosugi, and T. Suzuki, Phys. Chem. Chem. Phys. **13**, 413 (2011).

[125]T. Lewis, B. Winter, A. C. Stern, M. D. Baer, C. J. Mundy, D. J. Tobias, and J. C. Hemminger, J. Phys. Chem. B **115**, 9445 (2011).

[126]T. Lewis, M. Faubel, B. Winter, and J. C. Hemminger, Angew. Chem., Int. Ed. **50**, 10178 (2011).

[127]M. A. Brown, F. Vila, M. Sterrer, S. Thürmer, B. Winter, M. Ammann, J. J. Rehr, and J. A. van Bokhoven, J. Phys. Chem. Lett. **3**, 1754 (2012).

[128]N. L. Prisle, N. Ottosson, G. Öhrwall, J. Söderström, M. Dal Maso, and O. Björneholm, Atmos. Chem. Phys. **12**, 12227 (2012).

[129]I. Josefsson, S. K. Eriksson, N. Ottosson, G. Öhrwall, H. Siegbahn, A. Hagfeldt, H. Rensmo, O. Björneholm, and M. Odelius, Phys. Chem. Chem. Phys. **15**, 20189 (2013).

[130]M. A. Brown, A. Beloqui Redondo, M. Sterrer, B. Winter, G. Pacchioni, Z. Abbas, and J. A. van Bokhoven, Nano Lett. **13**, 5403 (2013).

[131]A. M. Margarella, K. A. Perrine, T. Lewis, M. Faubel, B. Winter, and J. C. Hemminger, J. Phys. Chem. C **117**, 8131 (2013).

[132]K. Nishizawa, K. Ohshimo, and T. Suzuki, J. Chin. Biochem. Soc. **60**, 1403 (2013).

[133]S. Thürmer, R. Seidel, M. Faubel, W. Eberhardt, J. C. Hemminger, S. E. Bradforth, and B. Winter, Phys. Rev. Lett. **111**, 173005 (2013).

[134]J. G. Pruyne, M.-T. Lee, C. Fábri, A. Beloqui Redondo, A. Kleibert, M. Ammann, M. A. Brown, and M. J. Krisch, J. Phys. Chem. C **118**, 29350 (2014).

[135]W. Pokapanich, N. Ottosson, J. Söderström, O. Björneholm, and G. Öhrwall, ScienceAsia **40**, 290 (2014).

[136]J. Werner, J. Julin, M. Dalirian, N. L. Prisle, G. Öhrwall, I. Persson, O. Björneholm, and I. Riipinen, Phys. Chem. Chem. Phys. **16**, 21486 (2014).

[137]J. Werner, E. Wernersson, V. Ekholm, N. Ottosson, G. Öhrwall, J. Heyda, I. Persson, J. Söderström, P. Jungwirth, and O. Björneholm, J. Phys. Chem. B **118**, 7119 (2014).

[138]N. Kurahashi, S. Karashima, Y. Tang, T. Horio, B. Abulimiti, Y.-I. Suzuki, Y. Ogi, M. Oura, and T. Suzuki, J. Chem. Phys. **140**, 174506 (2014).

[139]Y.-I. Suzuki, K. Nishizawa, N. Kurahashi, and T. Suzuki, Phys. Rev. E **90**, 010302 (2014).

[140]O. Björneholm, J. Werner, N. Ottosson, G. Öhrwall, V. Ekholm, B. Winter, I. Unger, and J. Söderström, J. Phys. Chem. C **118**, 29333 (2014).

[141]N. K. Jena, I. Josefsson, S. K. Eriksson, A. Hagfeldt, H. Siegbahn, O. Björneholm, H. Rensmo, and M. Odelius, Chem. Eur. J. **21**, 4049 (2015).

[142]G. Öhrwall, N. L. Prisle, N. Ottosson, J. Werner, V. Ekholm, M.-M. Walz, and O. Björneholm, J. Phys. Chem. B **119**, 4033 (2015).

[143]M.-T. Lee, M. A. Brown, S. Kato, A. Kleibert, A. Türler, and M. Ammann, J. Phys. Chem. A **119**, 4600 (2015).

[144]R. Seidel, K. Atak, S. Thürmer, E. F. Aziz, and B. Winter, J. Phys. Chem. B **119**, 10607 (2015).

[145]M.-M. Walz, C. Caleman, J. Werner, V. Ekholm, D. Lundberg, N. L. Prisle, G. Öhrwall, and O. Björneholm, Phys. Chem. Chem. Phys. **17**, 14036 (2015).

[146]M.-T. Lee, F. Orlando, L. Artiglia, S. Chen, and M. Ammann, J. Phys. Chem. A **120**, 9749 (2016).

[147]M.-M. Walz, J. Werner, V. Ekholm, N. L. Prisle, G. Öhrwall, and O. Björneholm, Phys. Chem. Chem. Phys. **18**, 6648 (2016).

[148]J. Werner, M. Dalirian, M.-M. Walz, V. Ekholm, U. Wideqvist, S. J. Lowe, G. Öhrwall, I. Persson, I. Riipinen, and O. Björneholm, Environ. Sci. Technol. **50**, 7434 (2016).

[149]M. J. Makowski, R. P. Galhenage, J. Langford, and J. C. Hemminger, J. Phys. Chem. Lett. **7**, 1732 (2016).

[150]G. Olivieri, A. Goel, A. Kleibert, D. Cvetko, and M. A. Brown, Phys. Chem. Chem. Phys. **18**, 29506 (2016).

[151]G. Olivieri, A. Goel, and M. A. Brown, Chem. Commun. **52**, 9040 (2016).

[152]G. Olivieri and M. A. Brown, Top Catal. **59**, 621 (2016).

[153]L. Artiglia, J. Edebeli, F. Orlando, S. Chen, M.-T. Lee, P. Corral Arroyo, A. Gilgen, T. Bartels-Rausch, A. Kleibert, M. Vazdar, M. Andres Carignano, J. S. Francisco, P. B. Shepson, I. Gladich, and M. Ammann, Nat. Commun. **8**, 700 (2017).

[154]S. S. N. Lalithambika, K. Atak, R. Seidel, A. Neubauer, T. Brandenburg, J. Xiao, B. Winter, and E. F. Aziz, Sci. Rep. **7**, 40811 (2017).

[155]R. K. Lam, J. W. Smith, A. M. Rizzuto, O. Karslıoğlu, H. Bluhm, and R. J. Saykally, J. Chem. Phys. **146**, 094703 (2017).

[156]K. A. Perrine, K. M. Parry, A. C. Stern, M. H. C. Van Spyk, M. J. Makowski, J. A. Freites, B. Winter, D. J. Tobias, and J. C. Hemminger, Proc. Natl. Acad. Sci. U. S. A. **114**, 13363 (2017).

[157]R. Seidel, K. Kraffert, A. Kabelitz, M. N. Pohl, R. Kraehnert, F. Emmerling, and B. Winter, Phys. Chem. Chem. Phys. **19**, 32226 (2017).

[158]I. Unger, R. Seidel, S. Thürmer, M. N. Pohl, E. F. Aziz, L. S. Cederbaum, E. Muchová, P. Slavíček, B. Winter, and N. V. Kryzhevoi, Nat. Chem. **9**, 708 (2017).

[159]H. Ali, R. Seidel, M. N. Pohl, and B. Winter, Chem. Sci. **9**, 4511 (2018).

[160]V. Ekholm, M. Vazdar, P. E. Mason, E. Bialik, M.-M. Walz, G. Öhrwall, J. Werner, J.-E. Rubensson, P. Jungwirth, and O. Björneholm, J. Chem. Phys. **148**, 144508 (2018).

[161]V. Ekholm, C. Caleman, N. Bjärnhall Prytz, M.-M. Walz, J. Werner, G. Öhrwall, J.-E. Rubensson, and O. Björneholm, Phys. Chem. Chem. Phys. **20**, 27185 (2018).

[162]J. Werner, I. Persson, O. Björneholm, D. Kawecki, C.-M. Saak, M.-M. Walz, V. Ekholm, I. Unger, C. Valtl, C. Caleman, G. Öhrwall, and N. L. Prisle, Phys. Chem. Chem. Phys. **20**, 23281 (2018).

[163]G. Olivieri, K. M. Parry, R. D'Auria, D. J. Tobias, and M. A. Brown, J. Phys. Chem. B **122**, 910 (2018).

[164]M.-T. Lee, F. Orlando, M. Khabiri, M. Roeselová, M. A. Brown, and M. Ammann, Phys. Chem. Chem. Phys. **21**, 8418 (2019).

[165]H. Ali, R. Seidel, A. Bergmann, and B. Winter, J. Mater. Chem. A **7**, 6665 (2019).

[166]T. Lewis, B. Winter, S. Thürmer, R. Seidel, A. B. Stephansen, J. A. Freites, D. J. Tobias, and J. C. Hemminger, J. Phys. Chem. C **123**, 8160 (2019).

[167]Y. S. Blanco, Ö. Topel, É. G. Bajnóczi, J. Werner, O. Björneholm, and I. Persson, Phys. Chem. Chem. Phys. **21**, 12434 (2019).

[168]V. Carravetta, A. H. de Abreu Gomes, S. Monti, A. Mocellin, R. R. T. Marinho, O. Björneholm, H. Ågren, and A. Naves de Brito, J. Phys. Chem. B **123**, 3776 (2019).

[169]S. Karashima and T. Suzuki, J. Phys. Chem. B **123**, 3769 (2019).

[170]J. P. Bruce and J. C. Hemminger, J. Phys. Chem. B **123**, 8285 (2019).

[171]H. Fellner-Feldegg, H. Siegbahn, L. Asplund, P. Kelfve, and K. Siegbahn, J. Electron Spectrosc. Relat. Phenom. **7**, 421 (1975).

[172]B. Lindberg, L. Asplund, H. Fellner-Feldegg, P. Kelfve, H. Siegbahn, and K. Siegbahn, Chem. Phys. Lett. **39**, 8 (1976).

[173]H. Siegbahn, S. Svensson, and M. Lundholm, J. Electron Spectrosc. Relat. Phenom. **24**, 205 (1981).

[174] H. Siegbahn and M. Lundholm, J. Electron Spectrosc. Relat. Phenom. **28**, 135 (1982).

[175] H. Siegbahn, M. Lundholm, M. Arbman, and S. Holmberg, Phys. Scr. **27**, 241 (1983).

[176] H. Siegbahn, M. Lundholm, S. Holmberg, and M. Arbman, Phys. Scr. **27**, 431 (1983).

[177] M. Arbman, S. Holmberg, M. Lundholm, and H. Siegbahn, Chem. Phys. **81**, 113 (1983).

[178] H. Siegbahn, M. Lundholm, S. Holmberg, and M. Arbman, Chem. Phys. Lett. **110**, 425 (1984).

[179] H. Siegbahn, M. Lundholm, M. Arbman, and S. Holmberg, Phys. Scr. **30**, 305 (1984).

[180] M. Lundholm, H. Siegbahn, S. Holmberg, and M. Arbman, J. Electron Spectrosc. Relat. Phenom. **40**, 163 (1986).

[181] O. Bohman, P. Ahlberg, M. Lundholm, S. Holmberg, R. Moberg, M. Arbman, and H. Siegbahn, J. Chem. Soc., Chem. Commun. **1986**, 1105.

[182] S. Holmberg, R. Moberg, Z. C. Yuan, and H. Siegbahn, J. Electron Spectrosc. Relat. Phenom. **41**, 337 (1986).

[183] S. Holmberg, R. Moberg, O. Bohman, and H. Siegbahn, J. Phys. Colloq. **48**, C9 (1987).

[184] S. Holmberg, Z. C. Yuan, R. Moberg, and H. Siegbahn, J. Electron Spectrosc. Relat. Phenom. **47**, 27 (1988).

[185] R. Moberg, Z. C. Yuan, S. Holmberg, F. Bökman, P. Ahlberg, O. Bohman, and H. Siegbahn, J. Phys. Org. Chem. **2**, 417 (1989).

[186] M. Arbman, R. Moberg, S. Holmberg, U. I. Wahlgren, and H. O. G. Siegbahn, Int. J. Quantum Chem. **41**, 637 (1992).

[187] R. Moberg, F. Boekman, O. Bohman, and H. O. G. Siegbahn, J. Am. Chem. Soc. **113**, 3663 (1991).

[188] R. Moberg, F. Bökman, O. Bohman, and H. O. G. Siegbahn, J. Chem. Phys. **94**, 5226 (1991).

[189] F. Bökman, O. Bohman, and H. O. G. Siegbahn, Chem. Phys. Lett. **189**, 414 (1992).

[190] F. Bökman, O. Bohman, and H. O. G. Siegbahn, J. Phys. Chem. **96**, 2278 (1992).

[191] F. Bökman, O. Bohman, and H. O. G. Siegbahn, Acta Chem. Scand. **46**, 403 (1992).

[192] O. A. Baschenko, F. Bökman, O. Bohman, and H. O. G. Siegbahn, J. Electron Spectrosc. Relat. Phenom. **62**, 317 (1993).

[193] H. O. G. Siegbahn and S. Södergren, J. Electron Spectrosc. Relat. Phenom. **76**, 417 (1995).

[194] S. Södergren, O. Bohman, H. Tiangjing, and H. Siegbahn, Acta Chem. Scand. **53**, 737 (1999).

[195] C. Wang and H. Morgner, Microchim. Acta **171**, 415 (2010).

[196] C. Wang and G. G. Andersson, Surf. Sci. **605**, 889 (2011).

[197] C. Wang and H. Morgner, Surf. Interface Anal. **43**, 784 (2011).

[198] C. Wang and H. Morgner, Appl. Surf. Sci. **257**, 2291 (2011).

[199] H. Pohl, R. Manzoor, and H. Morgner, Surf. Sci. **618**, 12 (2013).

[200] J. Maibach, C. Xu, S. K. Eriksson, J. Åhlund, T. Gustafsson, H. Siegbahn, H. Rensmo, K. Edström, and M. Hahlin, Rev. Sci. Instrum. **86**, 044101 (2015).

[201] J. Maibach, I. Källquist, M. Andersson, S. Urpelainen, K. Edström, H. Rensmo, H. Siegbahn, and M. Hahlin, Nat. Commun. **10**, 3080 (2019).

[202] S. Ghosal, J. C. Hemminger, H. Bluhm, B. S. Mun, E. L. D. Hebenstreit, G. Ketteler, F. D. Ogletree, F. G. Requejo, and M. Salmeron, Science **307**, 563 (2005).

[203] M. J. Krisch, R. D'Auria, M. A. Brown, D. J. Tobias, C. Hemminger, M. Ammann, D. E. Starr, and H. Bluhm, J. Phys. Chem. C **111**, 13497 (2007).

[204] S. Ghosal, M. A. Brown, H. Bluhm, M. J. Krisch, M. Salmeron, P. Jungwirth, and J. C. Hemminger, J. Phys. Chem. A **112**, 12378 (2008).

[205] M. D. Baer, I.-F. W. Kuo, H. Bluhm, and S. Ghosal, J. Phys. Chem. B **113**, 15843 (2009).

[206] A. Křepelová, T. Huthwelker, H. Bluhm, and M. Ammann, ChemPhysChem **11**, 3859 (2010).

[207] M. H. Cheng, K. M. Callahan, A. M. Margarella, D. J. Tobias, J. C. Hemminger, H. Bluhm, and M. J. Krisch, J. Phys. Chem. C **116**, 4545 (2012).

[208] H. Tissot, G. Olivieri, J.-J. Gallet, F. Bournel, M. G. Silly, F. Sirotti, and F. Rochet, J. Phys. Chem. C **119**, 9253 (2015).

[209] H. Tissot, J.-J. Gallet, F. Bournel, G. Olivieri, M. G. Silly, F. Sirotti, A. Boucly, and F. Rochet, Top. Catal. **59**, 605 (2016).

[210] X. Kong, D. Castarède, A. Boucly, L. Artiglia, M. Ammann, T. Bartels-Rausch, E. S. Thomson, and J. B. C. Pettersson, J. Phys. Chem. C **124**, 5263 (2020).

[211] V. Schmidt, *Electron Spectrometry of Atoms Using Synchrotron Radiation* (Cambridge University Press, 2005), p. 149479592.

[212] N. Ottosson, M. Odelius, D. Spångberg, W. Pokapanich, M. Svanqvist, G. Öhrwall, B. Winter, and O. Björneholm, J. Am. Chem. Soc. **133**, 13489 (2011).

[213] N. Ottosson, G. Öhrwall, and O. Björneholm, Chem. Phys. Lett. **543**, 1 (2012).

[214] S. Thürmer, M. Ončák, N. Ottosson, R. Seidel, U. Hergenhahn, S. E. Bradforth, P. Slavíček, and B. Winter, Nat. Chem. **5**, 590 (2013).

[215] R. Guillemin, S. Sheinerman, R. Püttner, T. Marchenko, G. Goldsztejn, L. Journel, R. K. Kushawaha, D. Céolin, M. N. Piancastelli, and M. Simon, Phys. Rev. A **92**, 012503 (2015).

[216] P. van der Straten, R. Morgenstern, and A. Niehaus, Z. Phys. D: At., Mol. Clusters **8**, 35 (1988).

[217] S. A. Sheinerman and V. Schmidt, J. Phys. B: At., Mol. Opt. Phys. **30**, 1677 (1997).

[218] F. Williams, S. P. Varma, and S. Hillenius, J. Chem. Phys. **64**, 1549 (1976).

[219] M. N. Pohl, E. Muchová, R. Seidel, H. Ali, Š. Sršeň, I. Wilkinson, B. Winter, and P. Slavíček, Chem. Sci. **10**, 848 (2019).

[220] S. Hofmann, *Auger- and X-Ray Photoelectron Spectroscopy in Materials Science*, Springer Series in Surface Sciences (Springer Berlin Heidelberg, Berlin, Heidelberg, 2013), Vol. 49.

[221] *Practical Surface Analysis*, 2nd ed., edited by D. Briggs and M. P. Seah (Wiley; Salle + Sauerländer, Chichester; New York; Aarau, 1990).

[222] R. Signorell, Phys. Rev. Lett. **124**, 205501 (2020).

[223] J. J. Yeh and I. Lindau, At. Data Nucl. Data Tables **32**, 1 (1985).

[224] J. H. Scofield, J. Electron Spectrosc. Relat. Phenom. **8**, 129 (1976).

[225] J. Söderström, N. Mårtensson, O. Travnikova, M. Patanen, C. Miron, L. J. Sæthre, K. J. Børve, J. J. Rehr, J. J. Kas, F. D. Vila, T. D. Thomas, and S. Svensson, Phys. Rev. Lett. **108**, 193005 (2012).

[226] G. Olivieri, K. M. Parry, C. J. Powell, D. J. Tobias, and M. A. Brown, J. Chem. Phys. **144**, 154704 (2016).

[227] C. Powell, NIST Electron Effective Attenuation Length Database, NIST Standard Reference Database No. 82, 2001.

[228] M. Michaud, A. Wen, and L. Sanche, Radiat. Res. **159**, 3 (2003).

[229] H. Shinotsuka, B. Da, S. Tanuma, H. Yoshikawa, C. J. Powell, and D. R. Penn, Surf. Interface Anal. **49**, 238 (2017).

[230] H. T. Nguyen-Truong, J. Phys.: Condens. Matter **30**, 155101 (2018).

[231] SESSA is a free software from the NIST, that allows to perform Monte-Carlo simulations of XPS spectra. See Werner *et al.*?.

[232] G. Olivieri, K. M. Parry, C. J. Powell, D. J. Tobias, and M. A. Brown, Phys. Chem. Chem. Phys. **19**, 6330 (2017).

[233] P. Jungwirth and D. J. Tobias, J. Phys. Chem. B **106**, 6361 (2002).

[234] K. L. Reid, Annu. Rev. Phys. Chem. **54**, 397 (2003).

[235] S. Gozem, R. Seidel, U. Hergenhahn, E. Lugovoy, B. Abel, B. Winter, A. I. Krylov, and S. E. Bradforth, J. Phys. Chem. Lett. **11**, 5162 (2020).

[236] B. A. Wellen, E. A. Lach, and H. C. Allen, Phys. Chem. Chem. Phys. **19**, 26551 (2017).

[237] M. F. Ruiz-Lopez, J. S. Francisco, M. T. C. Martins-Costa, and J. M. Anglada, Nat. Rev. Chem. **4**, 459 (2020).

[238] K. R. Siefermann, Y. Liu, E. Lugovoy, O. Link, M. Faubel, U. Buck, B. Winter, and B. Abel, Nat. Chem. **2**, 274 (2010).

[239] Y. Tang, H. Shen, K. Sekiguchi, N. Kurahashi, T. Mizuno, Y.-I. Suzuki, and T. Suzuki, Phys. Chem. Chem. Phys. **12**, 3653 (2010).

[240] A. Lübcke, F. Buchner, N. Heine, I. V. Hertel, and T. Schultz, Phys. Chem. Chem. Phys. **12**, 14629 (2010).

[241] M. H. Elkins, H. L. Williams, A. T. Shreve, and D. M. Neumark, Science **342**, 1496 (2013).

07 May 2025 10:15:31

[242]T. Suzuki, J. Chem. Phys. **151**, 090901 (2019).

[243]See https://www.helmholtz-berlin.de/forschung/oe/em/materialentwicklung/research/lidux_en.html for example the LIDUX facility at HZB.

[244]L. Barreau, A. D. Ross, S. Garg, P. M. Kraus, D. M. Neumark, and S. R. Leone, Sci. Rep. **10**, 5773 (2020).

[245]W. Widdra, D. Bröcker, T. Gießel, I. V. Hertel, W. Krüger, A. Liero, F. Noack, V. Petrov, D. Pop, P. M. Schmidt, R. Weber, I. Will, and B. Winter, Surf. Sci. **543**, 87 (2003).

[246]M. Marsi, M. E. Couprie, L. Nahon, D. Garzella, T. Hara, R. Bakker, M. Billardon, A. Delboulbé, G. Indlekofer, and A. Taleb-Ibrahimi, Appl. Phys. Lett. **70**, 895 (1997).

[247]J. D. Koralek, J. B. Kim, P. Brůža, C. B. Curry, Z. Chen, H. A. Bechtel, A. A. Cordones, P. Sperling, S. Toleikis, J. F. Kern, S. P. Moeller, S. H. Glenzer, and D. P. DePonte, Nat. Commun. **9** (2018).

[248]Presentation of the method on the author's web page: https://www.fhi.mpg.de/236287/experimental-methods.

07 May 2025 10:15:31